report no. 80HV007
july 1980

prepared for MSFC
under contract
no. NAS8-33573

FINAL REPORT ANALYSIS AND CALCULATION OF MACROSEGREGATION IN A CASTING INGOT

volume I - formulation and analysis

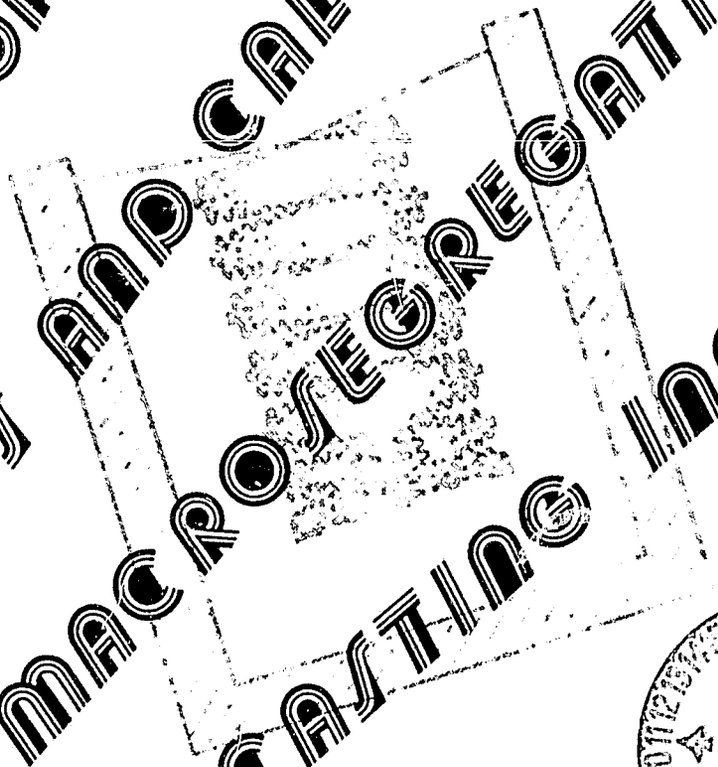

prepared by
the General Electric Co
huntsville operations
of the space division
huntsville alabama

GENERAL ELECTRIC

REPORT NO: 80HV007
DATE: JULY 1980

MPS SOLIDIFICATION MODEL

VOLUME I: FORMULATION AND ANALYSIS

FINAL REPORT

ANALYSIS AND CALCULATION OF MACROSEGREGATION

IN A CASTING INGOT

PREPARED FOR MSFC

UNDER CONTRACT NO. NAS8-33573

PREPARED BY: Anna L. Maples
Anna L. Maples
Program Manager

David R. Poirier
Dr. David R. Poirier
Dept. of Metallurgical Engineering
University of Arizona

APPROVED BY: Lowell A. Kelly
Lowell A. Kelly, Manager
Huntsville Operations

TABLE OF CONTENTS

LIST OF ILLUSTRATIONS

SECTION 1 - INTRODUCTION

This report describes the physical and numerical formulation of a model for the horizontal solidification of a binary alloy. It can be applied, for example, to the case of steady-state solidification from two opposing walls in an ingot. The major purpose of the model is to calculate macrosegregation in a casting ingot which results from flow of interdendritic liquid during solidification. The flow, driven by solidification contractions and by gravity acting on density gradients in the interdendritic liquid, is modeled as flow through a porous medium. Section 2 defines the symbols used throughout this report. Section 3 contains the physical formulation of the problem leading to a set of equations which can be used to obtain: (1) the pressure field, (2) the velocity field, (3) mass flow and (4) solute flow in the solid plus liquid zone during solidification. With these established, the model calculates macrosegregation after solidification is complete. Section 4 presents the numerical techniques used to obtain solution on a computational grid. Section 5 contains results, evaluation of the results, and recommendations for future development of the model. Included are the macrosegregation and flow field predictions for tin-lead, aluminum-copper, and tin-bismuth alloys as well as comparisons of some of the predictions with published predictions or with empirical data.

The numerical model is the basis for algorithms used in a FORTRAN program which has been run on a Prime 400 computer system at Marshall Space Flight Center (MSFC) in Huntsville, Alabama. The program can be run in batch or interactive mode; the latter mode allows the user to interact with the model by changing process parameters or alloy, and by selecting graphical or tabular output for display on the terminal screen. The documentation for the FORTRAN code is Volume II of this report, and the operating manual is Volume III. Volumes I and III are self-contained in the sense that they describe the model and its operation without reference to the FORTRAN code; accordingly no programming or computer operation experience is needed to make use of the model.

SECTION 2 - NOMENCLATURE

$\vec{A} = (A_x, A_y)$	coefficient in the pressure equation, Eq. (3.4.3)
B	coefficient in the pressure equation, Eq. (3.4.3)
$\overline{C}$ (wt. pct.)	average composition defined by Eq. (3.2.4)
C_L (wt. pct.)	composition of interdendritic liquid
C_S (wt. pct.)	local average composition of solid during solidification, defined by Eq. (3.2.5)
C_S^* (wt. pct.)	composition of the solid at the solid-liquid interface
$\overline{C}_S$ (wt. pct.)	final local average composition, Eq. (3.5.1)
C_o (wt. pct.)	composition of liquid at the liquidus isotherm, i.e., composition of the alloy
g_E	volume fraction of eutectic liquid at the end of solidification
g_L, g_S	volume fraction of liquid, solid during solidification
$\vec{g}$ (cm/s^2)	gravitational acceleration
g (cm/s^2)	gravitational acceleration in the -y direction
k	equilibrium partition ratio
K (cm^2)	permeability
L (cm)	ingot height
M_{SSI}, M_{SOR}	maximum number of steady state or pressure iterations
N_i, N_j	number of mesh points in the x or y direction
p (dynes/cm^2)	pressure
$\hat{p}$ (dynes/cm^2)	modified pressure defined in Eq. (4.5.1)
p_o (dynes/cm^2)	atmospheric pressure
t (s)	time
t_E, t_L (s)	time at passage of the eutectic front and liquidus isotherm, respectively
T (^{o}C)	temperature
T_E (^{o}C)	eutectic temperature
T_L (^{o}C)	liquidus temperature at composition C_o
U (cm/s)	isotherm velocity
$\vec{V}$ (cm/s)	velocity of the interdendritic fluid
V_x, V_y (cm/s)	x- and y- components of $\vec{V}$
x (cm)	horizontal distance from the chill face, see Figure 3.2
Δx (cm)	grid spacing in the x- direction
x_E, x_L (cm)	positions of the eutectic and liquidus isotherms, respectively
y (cm)	distance from the bottom of the ingot
Δy (cm)	grid spacing in y- direction

γ (cm^2)	permeability coefficient
E_{SSI}, E_{SOR}	convergence bounds; see Section 4.8
μ ($g/(cm \cdot s)$)	viscosity
$\overline{\rho}$ (g/cm^3)	average density defined by Eq. (3.2.2)
ρ_L (g/cm^3)	density of the interdendritic liquid
ρ_S (g/cm^3)	density of the primary solid phase
ρ_{LE}, ρ_{SE} (g/cm^3)	densities of the eutectic liquid and solid, respectively
ρ_{LO} (g/cm^3)	density of the liquid at the liquidus isotherm

SECTION 3 - PHYSICAL DESCRIPTION OF THE MODEL

3.1 PROBLEM DEFINITION

Figure 3.1 shows an ingot of a binary alloy undergoing horizontal solidification from chill faces located at opposite sides of an insulated rectangular mold. The mold is oriented so that the gravity force is in the y-direction as shown, with no component normal to the x-y plane. Initially the contents are liquid with uniform composition C_o. As heat is extracted through the chill faces, the alloy solidifies bidirectionally from the chills and toward the centerline. It is assumed that dendritic freezing takes place with a zone containing both solid and liquid phases (i.e., the S/L zone) which moves through the ingot ahead of the eutectic isotherms. Shrinkage-and gravity-driven convection within these S/L zones causes non-uniformities, known as macrosegregation, in the final local average composition after solidification, $\overline{C}_s$. The relationship between interdendritic fluid flow and macrosegregation was first described and demonstrated in references 3-5 for flow due to solidification contraction only, and later for flow driven by gravity, in addition to solidification shrinkages in references 1, 2, and 6. The solidification model described below calculates the final local average composition after solidification by solving the hydrodynamic equations for the flow of interdendritic liquid within the limitations of several assumptions.

The methods used here are similar to those of references 1 and 2 for macrosegregation resulting from steady-state solidification. The mold shown in Figure 3.1 is symmetric about the centerline, so it is sufficient to treat only the left side of the ingot. Because there is no body force normal to the x-y plane, the flow in the S/L zone is two-dimensional. Nevertheless, much of the analytical development will be independent of the coordinate system and dimensionality of the S/L zone. As defined in reference 3, "unidirectional" solidification implies unidirectional heat flow with planar isotherms, so that the S/L zone is rectangular and the temperature gradient has no y component. In steady-state solidification the isotherms move through the ingot at a constant velocity, thus the geometry of the mushy zone and the temperature distribution within the S/L zone are constant in time. The macrosegregation resulting from steady-state solidification does not vary in the direction of heat flow; the final local average composition is a function only of vertical distance through the ingot. The interdendritic fluid flow is driven both by shrinkage due to

solidification contraction and liquid contraction during solidification, and by gravity acting on a fluid of variable density. The density gradient results from thermal gradients and more so from solute concentration gradients which must exist in the liquid within the S/L zone. Flow resulting from the latter situation has been termed concentration-driven convection, and in references 1, 2, 6 and 7 it has been shown to be a major contributing factor in the formation of channel-type segregates often called "freckles". A fundamental assumption of the solidification model is no movement of the solid phase, so that the calculations cannot predict macrosegregation profiles for ingots in which freckles occur, although the conditions for and the location of the onset of freckle formation can be be predicted. The flow of interdendritic liquid is modeled as flow through a porous medium where the volume fraction available for flow is the local volume fraction of liquid during solidification. The movement of the S/L zone, the temperature field within the mushy zone, the liquid density as a function of composition and temperature, and the phase diagram (solid-liquid equilibria) for the binary alloy are assumed; the pressure field, velocity field, and macrosegregation are calculated.

3.2 FLOW EQUATIONS

Because the rate of isotherm movement is used as input to the solidification analysis and because no convection in the bulk liquid is assumed, the analysis can be restricted to the processes within the S/L zone and the solute flow at the boundaries of the S/L zone. The coordinate system defined in the S/L zone is shown in Figure 3.2. The coordinates of any point (x, y) in the S/L zone are fixed relative to the ingot. The sides of the S/L zone at $x_E(t)$ and $x_L(t)$, the positions of the entectic isotherm and liquidus isotherms, respectively, move through the ingot with a constant velocity U. The analysis leading to a solidification model is based upon the concept of a volume element within the S/L zone which is small enough to be treated as a differential element, yet large enough so that the volume fraction solid within it is equal to the local average. The volume element concept is developed in reference 3. There is no solid phase movement into or out of the cell; there is no mass flux into or out of the element by diffusion; temperature and liquid density vary only differentially across the cell at any time. With these assumptions conversation of mass within the volume element is written

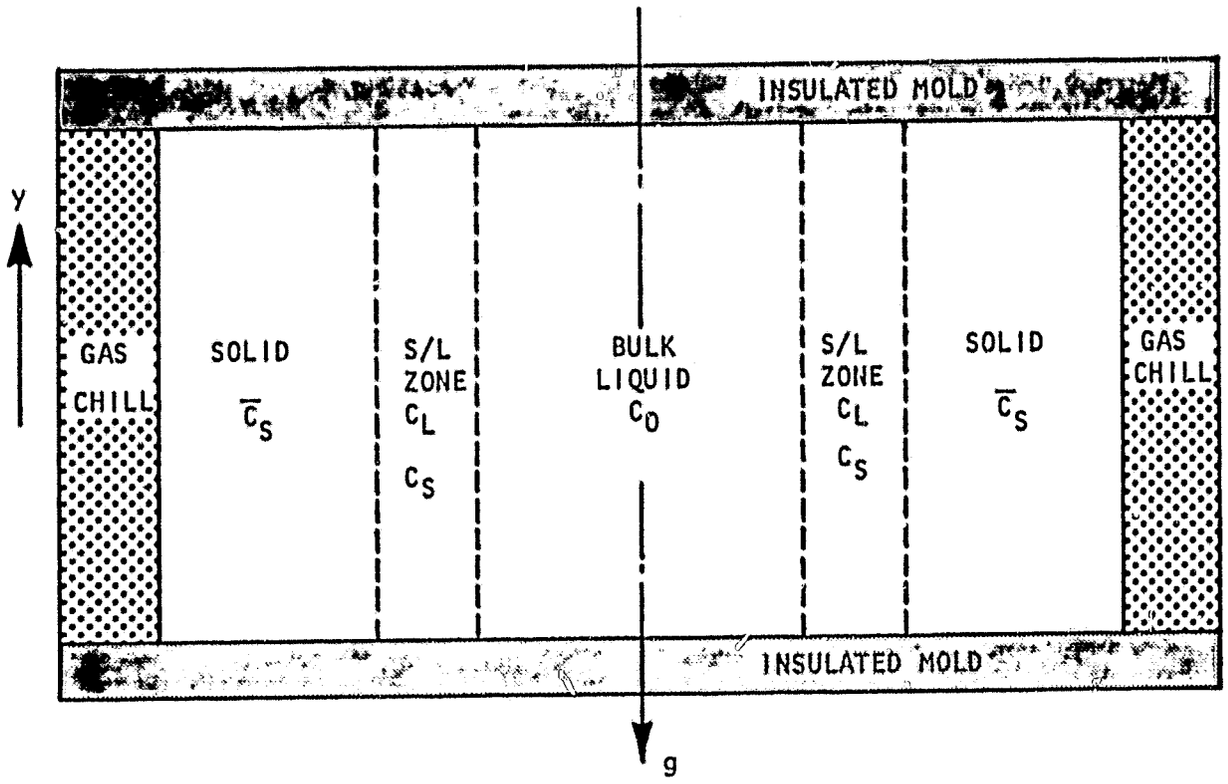

Figure 3.1. Horizontal Bidirectional Solidification

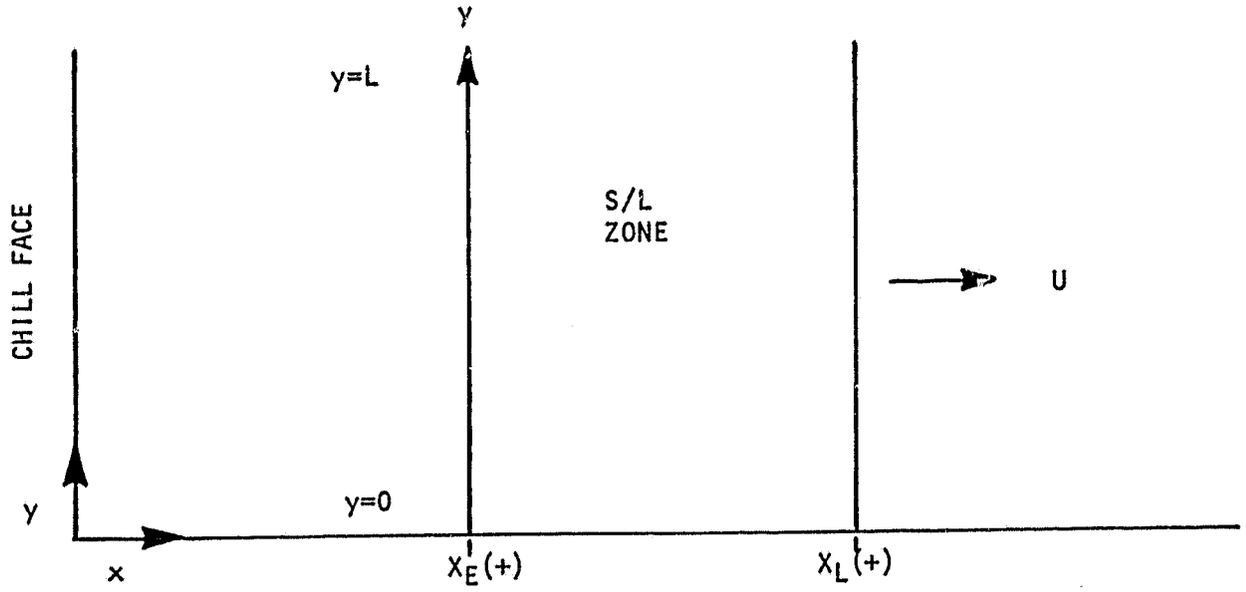

Figure 3.2. Coordinate System

$$\frac{\partial \overline{\rho}}{\partial t} = - \nabla \cdot \rho_L g_L \vec{V}, \tag{3.2.1}$$

where $$\overline{\rho} = \rho_s g_s + \rho_L g_L. \tag{3.2.2}$$

(See Section 2 for definitions of the symbols.) If solute enters or leaves the volume element only by liquid convection, if there is no solute diffusion within the solid phase, and if the composition of liquid within the volume element is uniform, then conservation of solute in the volume element is written

$$\frac{\partial}{\partial t} (\overline{C}\ \overline{\rho}) = - \nabla \cdot C_L \rho_L g_L \vec{V}, \tag{3.2.3}$$

where $$\overline{C}\ \overline{\rho} = C_s \rho_s g_s + C_L \rho_L g_L , \tag{3.2.4}$$

and C_S is the local average solid composition at time t, defined by

$$C_S(x,y,t) = \frac{1}{\rho_s g_s} \int_{t_L}^{t} \rho_s C_s^* (x,y,\hat{t}) \frac{\partial g_s}{\partial t} (x,y,\hat{t}) d\hat{t} \tag{3.2.5}$$

for t prior to passage of the eutectic front: $t_L \leq t < t_E$.

Mass fluxes at the edges of the S/L zone provide boundary conditions for the conservation equations. The top and bottom of the S/L zone are in contact with the mold walls so that there is no normal component of flow:

$$V_y = 0 \text{ at } y = 0 \text{ and } y = L \text{ for } x_E \leq x \leq x_L. \tag{3.2.6}$$

As described in reference 1, flow at the eutectic isotherm must compensate for solidification shrinkage or expansion of the eutectic mixture:

$$V_x = - \frac{\rho_{SE} - \rho_{LE}}{\rho_{LE}} U \quad \text{at } x = x_E \text{ for } 0 \leq y \leq L. \tag{3.2.7}$$

Since it is assumed that there is no convection in the bulk liquid, then

$$V_y = 0 \quad \text{at } x = X_L \text{ for } 0 \leq y \leq L. \tag{3.2.8}$$

Additional conditions at the liquidus isotherm are

$$C_L = C_0 \text{ and } g_L = 1 \text{ at } x = x_L \text{ for } 0 \leq y \leq L. \tag{3.2.9}$$

Darcy's Law for flow through a porous medium is used to describe the flow of the interdendritic liquid in the S/L zone; thus

$$\vec{V} = \frac{-K}{\mu g_L} (\nabla p + \rho_L \vec{g}), \tag{3.2.10}$$

where μ is the viscosity of the liquid and K is the permeability given here, as in references 1 and 2, by

$$K = \gamma g_L^2 \tag{3.2.11}$$

with γ a constant. This form of the permeability function is isotropic; i.e., there is no directional preference in the resistance to flow.

In addition to the assumptions of steady-state, unidirectional solidification, which lead to planar isotherms moving with a constant velocity, a constant horizontal temperature gradient is assumed. Then the temperature field in the mushy zone is given by

$$T(x,y,t) = T_E + \frac{T_L - T_E}{x_L - x_E}(x - x_E) \tag{3.2.12}$$

for $x_E \leq x \leq x_L$ and $0 \leq y \leq L$, as shown in Figure 3.4. The steady-state assumption now gives the isotherm velocity

$$U = - \frac{\partial T}{\partial t} \Big/ \frac{\partial T}{\partial x} = - \frac{\partial T}{\partial t} \Big/ \left(\frac{T_L - T_E}{x_L - x_E}\right). \tag{3.2.13}$$

Equations (3.2.12) and (3.2.13) show that the temperature field and isotherm movement are determined upon specification of the cooling rate, $\partial T/\partial t$, and the mushy zone width, $(x_L - x_E)$. The liquid in the volume element is assumed to be in equilibrium with the solid at the solid-liquid interface so that the phase diagram relates liquid composition to temperature in the volume element. As shown in Figure 3.3, the liquidus of the phase diagram is approximated by a straight line, and the composition of the interface solid is given by

$$C_S^* = kC_L, \tag{3.2.14}$$

where k is the equilibrium partition ratio. C_L and $\partial C_L/\partial t$ can thus be calculated as functions of temperature by

$$C_L(T) = C_E + \frac{dC_L}{dT}(T-T_E) \text{ and } \frac{\partial C_L}{\partial t} = \frac{dC_L}{dT}\frac{\partial T}{\partial t} \qquad (3.2.15)$$

where C_E, T_E and dC_L/dT are taken from the alloy phase diagram. The resultant linear variation of C_L through the S/L zone is shown in Figure 3.4. Liquid density is a function of temperature and composition, but the equilibrium assumption allows density to be written as a function of composition only. References 1 and 2 have shown that the density of the interdendritic liquid can be approximated by a linear function of composition and that the density of the primary solid phase is approximately constant in the solidification temperature range. Thus liquid density and $\partial \rho_L/\partial t$ can be calculated by

$$\rho_L(C_L) = \rho_{LE} + \frac{d\rho_L}{dC_L}(C_L-C_E) \text{ and } \frac{\partial \rho_L}{\partial t} = \frac{d\rho_L}{dC_L}\frac{\partial C_L}{\partial t}. \qquad (3.2.16)$$

ρ_S can be considered constant, and the densities of the solid and liquid phases are completely specified by known values of ρ_S, ρ_{SE}, $d\rho_L/dC_L$, and ρ_{LE}. The variation of ρ_L across the S/L zone is shown in Figure 3.4 where ρ_L increases during solidification. Some alloys have a decrease of liquid density during solidification and they can be treated, as well, providing the correct sign for $d\rho_L/dC_L$ is used.

An equation used to relate g_S and g_L is provided by the assumption of no pore formation:

$$g_S + g_L = 1, \quad \text{or} \quad \frac{\partial g_S}{\partial t} = -\frac{\partial g_L}{\partial t}. \qquad (3.2.17)$$

Equations (3.2.1) through (3.2.17) and the associated assumptions completely describe the solidification model. However, the solution for the velocity field and local fraction liquid can be simplified if the information above is used to derive two more equations which replace the continuity equations in the solution process. These equations are derived in Sections 3.3 and 3.4.

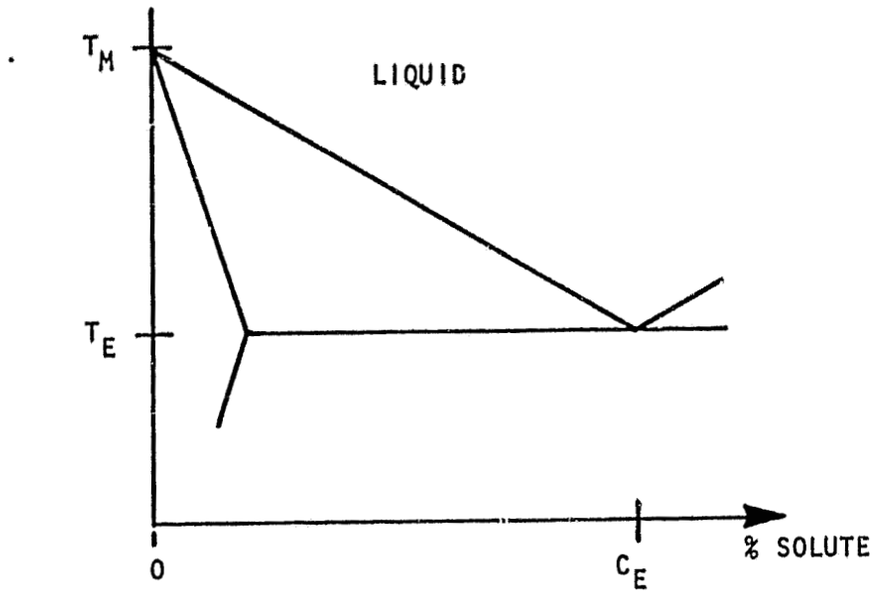

Figure 3.3. Simplified Phase Diagram

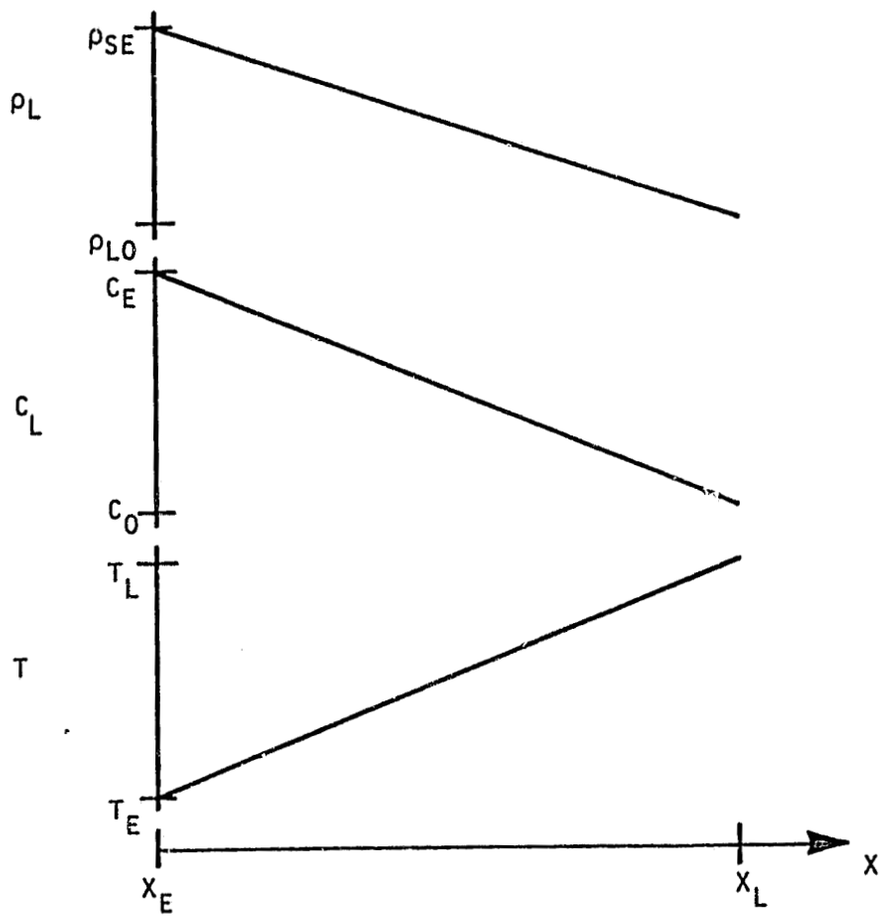

Figure 3.4. Linear Variation of T, C_L, and ρ_L

3.3 LOCAL SOLUTE REDISTRIBUTION EQUATION

The mass and solute conservation equations can be combined to get an equation, derived originally in reference 3, that gives the local fraction liquid in terms of the local velocity and the local liquid composition. By expanding the right side of Equation (3.2.3) and substituting Equations (3.2.1) and (3.2.2), we arrive at

$$-\nabla\cdot C_L\rho_L g_L\vec{V} = C_L\frac{\partial}{\partial t}(\rho_L g_L) - C_L\rho_S\frac{\partial g_L}{\partial t} - \rho_L g_L\vec{V}\cdot\nabla C_L. \qquad (3.3.1)$$

When Equation (3.2.5) is differentiated, there results

$$\frac{\partial}{\partial t}(C_S) = -\frac{1}{g_S}\frac{\partial g_S}{\partial t}C_S + \frac{1}{g_S}C_S^*\frac{\partial g_S}{\partial t} = \frac{1}{g_S}\frac{\partial g_S}{\partial t}(C_S^*-C_S). \qquad (3.3.2)$$

Expanding the left side of Equation (3.2.3) and substituting Equations (3.2.14), (3.2.17) and (3.3.2) leads to

$$\frac{\partial}{\partial t}(\overline{C}\,\overline{\rho}) = -kC_L\rho_S\frac{\partial g_L}{\partial t} + \rho_L g_L\frac{\partial C_L}{\partial t} + C_L\frac{\partial}{\partial t}(\rho_L g_L). \qquad (3.3.3)$$

Finally, Equations (3.3.1) and (3.3.3) are substituted into Equation (3.2.3), giving

$$\frac{1}{g_L}\frac{\partial g_L}{\partial t} = -\left(\frac{1}{1-k}\right)\frac{\rho_L}{\rho_S}\frac{1}{C_L}\left(\frac{\partial C_L}{\partial t} + \vec{V}\cdot\nabla C_L\right). \qquad (3.3.4)$$

Since the liquid composition and temperature are directly related (see Equation 3.2.15), then

$$\nabla C_L = \frac{\partial C_L}{\partial T}\nabla T \text{ and } \frac{\partial C_L}{\partial t} = \frac{\partial C_L}{\partial T}\frac{\partial T}{\partial t}, \qquad (3.3.5)$$

and Equation (3.3.4) becomes

$$\frac{1}{g_L}\frac{\partial g_L}{\partial t} = -\left(\frac{1}{1-k}\right)\frac{\rho_L}{\rho_S}\left(1 + \frac{\vec{V}\cdot\nabla T}{\frac{\partial T}{\partial t}}\right)\frac{1}{C_L}\frac{\partial C_L}{\partial t}. \qquad (3.3.6)$$

Equation (3.3.6) is called the local solute redistribution equation.

3.4 PRESSURE EQUATION

Numerical solution of the solidification model equations can be facilitated by replacing the mass conservation equation with an elliptic equation for pressure. Using Equations (3.2.2) and (3.2.17) and the assumption of constant solid density to expand the left side of Equation (3.2.1) gives:

$$\frac{\partial \bar{\rho}}{\partial t} = (\rho_L - \rho_S) \frac{\partial g_L}{\partial t} + g_L \frac{\partial \rho_L}{\partial t} . \tag{3.4.1}$$

The pressure equation results from substituting Equations (3.2.10) and (3.4.1) into Equation (3.2.1):

$$\nabla \cdot \left[\frac{k\rho_L}{\mu} (\nabla p + \rho_L \vec{g}) \right] - (\rho_L - \rho_S) \frac{\partial g_L}{\partial t} - g_L \frac{\partial \rho_L}{\partial t} = 0. \tag{3.4.2}$$

Equation (3.4.2) can be written in the form:

$$\nabla^2 p + \vec{A} \cdot \nabla p + B = 0 \tag{3.4.3}$$

with
$$\vec{A} = \frac{\mu}{K\rho_L} \nabla \left(\frac{K\rho_L}{\mu} \right), \tag{3.4.4}$$

and
$$B = \frac{\mu}{K\rho_L} \left[\nabla \cdot \left(\frac{K\rho_L}{\mu} \rho_L \vec{g} \right) - (\rho_L - \rho_S) \frac{\partial g_L}{\partial t} - g_L \frac{\partial \rho_L}{\partial t} \right] . \tag{3.4.5}$$

As discussed in Section 4.5, several numerical techniques are available for solution of equations with the form of Equation (3.4.3).

Conditions (3.2.6) through (3.2.8) can be rewritten to provide boundary conditions on pressure at all sides of the S/L zone. Substituting Equation (3.2.6) for V_y in Darcy's Law, Equation (3.2.10), gives

$$\frac{\partial p}{\partial y} = - \rho_L g \quad \text{at } y = 0 \text{ and } y = L \text{ for } x_L \leq x \leq x_E, \tag{3.4.6}$$

and substituting Equation (3.2.7) for V_x in Equation (3.2.10) gives

$$\frac{\partial p}{\partial x} = \frac{\mu g_L}{K} \frac{\rho_{SE} - \rho_{LE}}{\rho_{LE}} U \quad \text{at } x = x_E \text{ for } 0 \leq y \leq L. \tag{3.4.7}$$

If there is no convection in the bulk liquid, then

$$p = p_o + \rho_{L_o} g\,(L-y) \text{ at } x = x_L \text{ for } 0 \le y \le L. \tag{3.4.8}$$

3.5 MACROSEGREGATION

After solidification is complete at a point (x,y) in a casting, the final local average composition is given by

$$\overline{C}_S(x,y) = \frac{\rho_S \int_{t_L}^{t_E} C_S^*(x,y,t)\,dg_S(x,y,t) + \rho_{SE} g_E C_E}{\rho_S(1-g_E) + \rho_{SE} g_E} \tag{3.5.1}$$

where the liquidus isotherm passes the point (x,y) at time t_L and the eutectic front passes at t_E. The integral term accounts for microsegregation within the dendritic solid and the second term in the numerator accounts for the solute in the solidified eutectic mixture.

For steady-state solidification $\overline{C}_S$ is a function only of y, and the integral in Equation 3.5.1 is equal to the same integral taken between the limits x_L to x_E at a fixed time t. Macrosegregation as a function of height in the ingot is given by $\overline{C}_S(y) - C_o$.

3.6 SUMMARY

The equations which constitute a complete description of the solidification model implemented in the computer program are as follows:

Local Solute Redistribution Equation

$$\frac{1}{g_L}\frac{\partial g_L}{\partial t} = -\left(\frac{1}{1-k}\right)\frac{\rho_L}{\rho_S}\left[1 + \frac{\vec{V}\cdot\nabla T}{\frac{\partial T}{\partial t}}\right]\frac{1}{C_L}\frac{\partial C_L}{\partial t} \tag{3.6.1}$$

with $$g_L = 1 \text{ at } x = x_L \text{ for } 0 \le y \le L. \tag{3.6.2}$$

Pressure Equation

$$\nabla^2 p + \vec{A}\cdot\nabla p + B = 0 \tag{3.6.3}$$

for $$\vec{A} = \frac{\mu}{K\rho_L}\nabla\left(\frac{K\rho_L}{\mu}\right), \tag{3.6.4}$$

and $$B = \frac{\mu}{K\rho_L}\left[\nabla\cdot\left(\frac{K\rho_L}{\mu}\rho_L\vec{g}\right) - (\rho_L-\rho_S)\frac{\partial g_L}{\partial t} - g_L\frac{\partial \rho_L}{\partial t}\right] \tag{3.6.5}$$

with $$\frac{\partial p}{\partial y} = -\rho_L g \text{ at } y = 0 \text{ and } y = L \text{ for } x_E \le x \le x_L, \tag{3.6.6}$$

$$\frac{\partial p}{\partial x} = \frac{\mu g_L}{K}\frac{\rho_{SE}-\rho_{LE}}{\rho_{LE}} U \text{ at } x = x_E \text{ for } 0 \le y \le L, \tag{3.6.7}$$

and $$p = p_o + \rho_{L_o} g\,(L-y) \text{ at } x = x_L \text{ for } 0 \le y \le L. \tag{3.6.8}$$

Porous Flow Model

$$\vec{V} = -\frac{K}{\mu g_L}(\nabla p + \rho_L \vec{g}) \tag{3.6.9}$$

$$K = \gamma g_L^2 \tag{3.6.10}$$

Temperature Field

$$T = T_E + \frac{T_L - T_E}{x_L - x_E}(x - x_E) \quad \text{for } x_E \le x \le x_L \tag{3.6.11}$$

$$U = -\frac{\partial T}{\partial t}\Big/\frac{\partial T}{\partial x} \tag{3.6.12}$$

Liquid Composition

$$C_L = C_E + \frac{dC_L}{dT}(T - T_E);\ \frac{\partial C_L}{\partial t} = \frac{dC_L}{dT}\frac{\partial T}{\partial t} \tag{3.6.13}$$

Liquid Density

$$\rho_L = \rho_{LE} + \frac{d\rho_L}{dC_L}(C_L - C_E);\ \frac{\partial \rho_L}{\partial t} = \frac{d\rho_L}{dC_L}\frac{dC_L}{dT}\frac{\partial T}{\partial t} \tag{3.6.14}$$

Final Composition

$$\bar{C}_S(y) = \frac{\rho_S \int_{x_L}^{x_E} kC_L dg_S + \rho_{SE} g_E C_E}{\rho_S(1-g_E) + \rho_{SE} g_E} \qquad (3.6.15)$$

The following data are required as input to the solidification model.

Phase Diagram: T_E, C_E, $\frac{dC_L}{dT}$, k

Alloy: C_o

Solidification Process: L, $(x_L - x_E)$, $\partial T/\partial t$, g

Density: ρ_{LE}, $d\rho_L/dC_L$, ρ_S, ρ_{SE}

Viscosity: μ

Permeability Coefficient: γ

Upon specification of these values, the description of a steady-state casting of a binary alloy is complete, and Equations (3.6.1) through (3.6.15) can be solved to yield the final local average composition as a function of vertical distance through the ingot. The following section describes the numerical analysis which is the basis of a computer program which performs such a calculation.

SECTION 4 - NUMERICAL METHODS

The equations presented in Section 3 require reformatting in a discrete form for solution on a digital computer. Numerical techniques applied to the continuous equations yield finite difference equations and procedures for calculation of their solution. This process involves selection of finite difference methods that are appropriate to the type of partial differential equation to be solved as well as systematic verification of the convergence of the discrete solution to the solution of the continuous equations. Although the last fifteen years have seen tremendous advances in the discipline of numerical analysis applied to fluid flow equations, there is as yet no standard approach to the process of solving a particular set of equations. Techniques that provide a valid solution to one problem can produce an invalid but physically plausible result when applied to a slightly different problem. For this reason the verification phase of the process is crucial: a "solution" should never be accepted merely because it has a qualitative physical explanation. Procedures for sufficient validation of a solution to a flow problem are even less routine than the selection of the solution technique; they require experience in recognizing the behavior of an invalid result as well as an understanding of the foundations of the numerical approximation process.

Beyond the necessity of finding numerical methods which produce a sufficiently accurate solution, the constraints of interactive computing on a time-shared mini-computer require the use of memory-efficient, rapidly-convergent techniques. Numerical methods applied in the context of batch computing on a large high-speed mainframe are frequently chosen for their ease of application and because of their familiarity; in an interactive mini-computer application such methods can cause excessively long response times. Thus the use of extremely small grid spacings and double precision arithmetic, standard "fixes" for inadequate numerical methods, are to be avoided in mini-computer applications in favor of numerical techniques that are more specifically tailored to the problem at hand.

The techniques described in this section have been implemented and validated in an interactive program on the Prime 400 at MSFC. Under heavy job-load conditions the response time for the primary calculation phase is less than five minutes.

4.1 COMPUTATIONAL GRID

The numerical solution is calculated on a rectangular grid covering the S/L zone as shown in Figure 4.1. The value of a function at a grid point is considered representative of the behavior of the function in the surrounding cell so that, for convergent numerical methods, the solution of the finite difference equations is close to the solution of the partial differential equations when the mesh spacing is sufficiently small. In the following discussion subscript notation indicates location in the mesh: for any function defined in the S/L zone,

$$f_{ij} = f(x_i, y_j)$$

where $x_i = x_E + (i-1)\Delta x$ for $i = 1, \ldots, N_i$,

and $Y_j = (j-1)\Delta y$ for $j = 1, \ldots, N_j$.

Δx and Δy are given by

$$\Delta x = \frac{x_L - x_E}{N_i - 1} \quad \text{and} \quad \Delta y = \frac{L}{N_j - 1} .$$

4.2 OVERVIEW OF SOLUTION PROCESS

The outline of the solution process is the same as the one used in reference 2. Details of each step may vary from those employed in reference 2 because of the difference in coordinate systems as well as the use of alternate numerical techniques. The solution steps are explained in detail in later subsections and the program modules containing the relevant code are indicated.

1. Read the program input as defined in subsection 3.6.
2. Calculate Γ, U, C_L, $\frac{\partial C_L}{\partial t}$, ρ_L and $\frac{\partial \rho_L}{\partial t}$ at each point in the S/L zone by evaluating equations (3.6.11) through (3.6.14).
3. Calculate an initial estimated distribution of g_L and $\frac{\partial g_L}{\partial t}$ using the analytic solution for the zero gravity case, equations (4.3.1), (4.3.2), and (3.6.1); evaluate K according to equation (3.6.10).
4. Calculate an initial estimated pressure solution from equations (4.5.12) and (4.3.2).
5. Evaluate the pressure equation coefficients, $\vec{A}$ and B as shown in subsection 4.4.

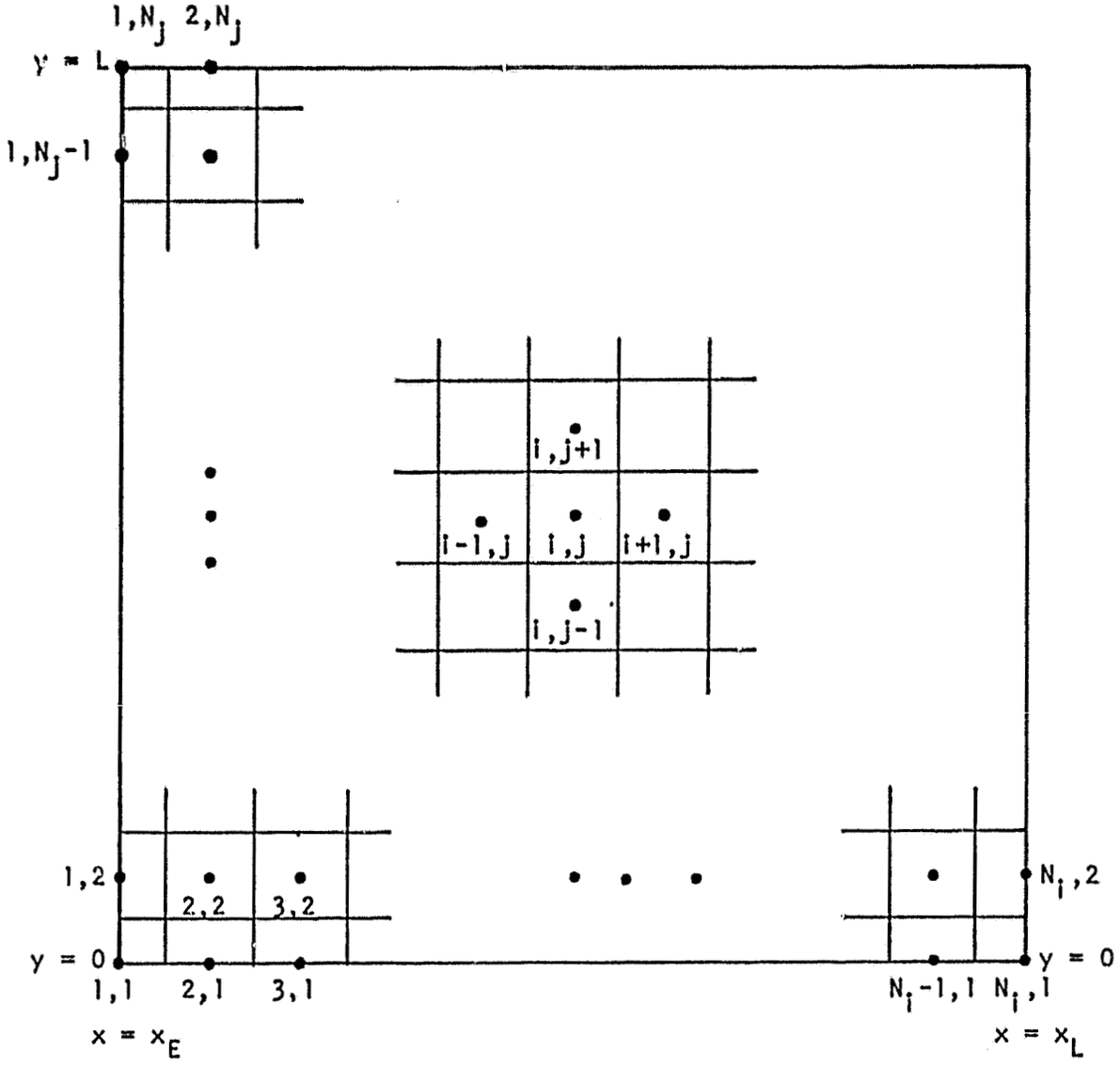

Figure 4.1. Computational Mesh

6. Solve the pressure equation using the relaxation technique discussed in subsection 4.5.
7. Use Darcy's Law as shown in subsection 4.6 to evaluate the velocity of the interdendritic flow.
8. Use the velocity calculated at step 7 in the local solute redistribution equation, as shown in subsection 4.7, to calculate new distributions of g_L and $\frac{\partial g_L}{\partial t}$; re-evaluate K by applying equation (3.6.10) at each point in the mesh.
9. Check convergence of the nonlinear system by applying the criteria described in subsection 4.8. If it has not converged and if freckling has not been detected, repeat steps 5 through 9.
10. Calculate the final local average composition.

4.3 INITIAL ESTIMATED SOLUTION

Starting the iterative calculation of the steady-state solution requires an estimate of g_L and $\frac{\partial g_L}{\partial t}$ to be used in generating the pressure equation coefficients for the first pass through steps 5 through 9. Although the initial estimated solution has no effect on the converged solution, convergence to the steady-state g_L, if one exists, can be speeded by starting the iteration with a good estimate of g_L. Hence the analytic solution for the case with no gravity force is used to estimate g_L. The only driving force in this case is shrinkage contraction so that the y-component of velocity is zero. The expressions for g_L, derived in reference 1, is:

$$g_L = \frac{C_L^{\alpha} + \left(\frac{\rho_s}{\rho_{se}} - 1\right) C_E^{\alpha}}{C_o^{\alpha} + \left(\frac{\rho_s}{\rho_{se}} - 1\right) C_E^{\alpha}} \qquad (4.3.1)$$

with $$\alpha = -\frac{1}{1-k} .$$

$\frac{\partial g_L}{\partial t}$ can be evaluated directly from equation (3.6.1) with Vy = 0 and

$$V_x = -\frac{g_L(\rho_s - \rho_L) + g_E(\rho_{SE} - \rho_s)}{\rho_L g_L} U. \qquad (4.3.2)$$

The initial estimated solution is calculated in subroutine EST.

4.4 EVALUATION OF THE PRESSURE EQUATION COEFFICIENTS

For general distributions of g_L there is no analytic form, so the gradient and divergence terms in $\vec{A}$ and B must be evaluated numerically. Comparison of centered finite difference formulas with evaluations of the analytic expressions available in the zero gravity case shown that differencing the logarithmic form of the spatial derivative terms is an order of magnitude more accurate than differencing the forms shown in equations (3.6.4) and (3.6.5). Using the logarithmic form provides a more accurate solution for a given mesh size, or it permits a coarser mesh in achieving a given accuracy, thus reducing computation time. The logarithmic forms of $\vec{A}$ and B subject to $\vec{g} = (o,g)$ are:

$$\vec{A} = \nabla\left[\ln\left(\frac{K\rho_L}{\mu}\right)\right] , \tag{4.4.1}$$

and

$$B = g\rho_L \frac{\partial}{\partial y}\left[\ln\left(\frac{K\rho_L^2}{\mu}\right)\right] - \frac{\mu}{K\rho_L}\left[(\rho_L-\rho_s)\frac{\partial g_L}{\partial t} + g_L \frac{\partial \rho_L}{\partial t}\right] . \tag{4.4.2}$$

Centered finite differences applied to these forms give:

$$(A_x)_{ij} \cong \left[\ln\left(\frac{K\rho_L}{\mu}\right)_{i+1,j} - \ln\left(\frac{K\rho_L}{\mu}\right)_{i-1,j}\right]/(2\Delta x) \tag{4.4.3}$$

for $1<i<N_i$ and $1\le j\le N_j$,

$$(A_y)_{ij} \cong \left[\ln\left(\frac{K\rho_L}{\mu}\right)_{i,j+1} - \ln\left(\frac{K\rho_L}{\mu}\right)_{i,j-1}\right]/(2\Delta y) \tag{4.4.4}$$

for $1\le i\le N_i$ and $1<j<N_j$,

and

$$\frac{\partial}{\partial y}\left[\ln\left(\frac{K\rho_L^2}{\mu}\right)\right]_{ij} \cong \left[\ln\left(\frac{K\rho_L^2}{\mu}\right)_{i,j+1} - \ln\left(\frac{K\rho_L^2}{\mu}\right)_{i,j-1}\right]/(2\Delta y) \tag{4.4.5}$$

for $1\le i\le N_i$ and $1<j<N_j$.

At the edges of the mesh centered differences cannot be used; the x-derivative terms are approximated by first order difference formulas of the form

$$\left(\frac{\partial f}{\partial x}\right)_{ij} \cong \pm (f_{i\pm1,j} - f_{ij})/\Delta x \quad \text{for } i=1,N_i \text{ and } 1\leq j\leq N_j, \tag{4.4.6}$$

and the y-derivative terms are approximated by second order difference formulas of the form

$$\left(\frac{\partial f}{\partial y}\right)_{ij} \cong \mp (3f_{ij} - 4f_{i,j\pm1} + f_{i,j\pm2})/(2\Delta y) \text{ for } j=1,N_j \text{ and } 1\leq i\leq N_i. \tag{4.4.7}$$

Subroutine PSETUP evaluates $\vec{A}$ and B.

4.5 SOLUTION OF THE PRESSURE EQUATION

Because atmospheric pressure, p_o, is very large compared to the pressure variations in the S/L zone, the accuracy of a numerical solution for total pressure would be considerably less than that of a solution for $p-p_o$. Similarly, the large hydrostatic pressure near the bottom of the S/L zone causes an unacceptable loss of significance in the calculation of $\frac{\partial}{\partial x}(p-p_o)$ during the the evaluation of V_x. These inaccuracies, inherent in direct solution for p, can be avoided by solving a modified pressure equation for

$$\hat{p} = p - p_o - \rho_{Lo} g(L-y) \tag{4.5.1}$$

where $\rho_{Lo} g(L-y)$ is the bulk fluid hydrostatic pressure. $\hat{p}$ is the solution of

$$\nabla^2 \hat{p} + \vec{A}\cdot\nabla\hat{p} + \hat{B} = 0 \tag{4.5.2}$$

where $\vec{A}$ is unchanged and

$$\hat{B} = B - \rho_{Lo} g A_y. \tag{4.5.3}$$

The boundary conditions for equation (4.5.2) are

$$\frac{\partial \hat{p}}{\partial y} = (\rho_{Lo} - \rho_L) g \text{ at } y=0 \text{ and } y=L \text{ for } x_L \leq x \leq x_E, \tag{4.5.4}$$

$$\frac{\partial \hat{p}}{\partial y} = \frac{\mu g_L}{K} \frac{\rho_{SE} - \rho_{LE}}{\rho_{LE}} U \text{ at } x = x_E \text{ for } 0\leq y\leq L, \tag{4.5.5}$$

$$\hat{p} = 0 \text{ at } x = x_L \text{ for } 0 \leq y \leq L. \qquad (4.5.6)$$

Standard solution procedures exist for linear elliptic equations such as equation (4.5.2). Iterative techniques have been preferred for a number of years, although fast direct (non-iterative) methods have been developed recently for problems with a large number of mesh points (references 8 and 9). Direct methods can be cumbersome to apply, especially if there are derivative boundary conditions or first order terms in the elliptic equation. Iterative techniques tend to converge slowly, but they are applicable to the most general form of the elliptic problem. The solidification model requires only a relatively small number of mesh points, it has derivative conditions at three boundaries, and it has a first order pressure term. Consequently, the iterative technique known as successive overrelaxation (SOR), or the accelerated Gauss-Seidel scheme, was applied to the pressure equation, and the strategy developed in reference 10 was used to speed convergence by dynamic estimation of the optimum acceleration parameter.

The recursive formula for the (n+1)st iterate of $\hat{p}$ according to the method of successive overrelaxation (reference 8, p. 468) is

$$\begin{aligned} p_{ij}^{n+1} &= (1-\omega)\hat{p}_{ij} \qquad (4.5.7) \\ &+ \omega\Big[\theta_x(\hat{p}_{i+1,j}^{\,n} + \hat{p}_{i-1,j}^{\,n+1}) + \theta_y(\hat{p}_{i,j+1}^{\,n} + \hat{p}_{i,j-1}^{\,n+1}) \\ &+ (\alpha_x)_{ij}(\hat{p}_{i+1,j}^{\,n} - \hat{p}_{i-1,j}^{\,n+1}) + (\alpha_y)_{ij}(\hat{p}_{i,j+1}^{\,n} + \hat{p}_{i,j-1}^{\,n+1}) + \delta^2 B_{ij}\Big] \end{aligned}$$

for $1 \leq i \leq N_j$ and $1 \leq j \leq N_j$

where
$$\theta_x = \frac{\Delta y^2}{2(\Delta x^2 + \Delta y^2)}, \qquad (\alpha_x)_{ij} = \frac{1}{2}\frac{\delta^2}{\Delta x}(A_x)_{ij},$$

$$\theta_y = \frac{\Delta x^2}{2(\Delta x^2 + \Delta y^2)}, \qquad (\alpha_y)_{ij} = \frac{1}{2}\frac{\delta^2}{\Delta y}(A_y)_{ij},$$

$$\delta^2 = \frac{\Delta x^2 \Delta y^2}{2(\Delta x^2 + \Delta y^2)},$$

and ω is the relaxation parameter described below. The restriction $i < N_j$ is the

boundary condition at $x = x_L$: $\hat{p}_{N_i,1}$ does not change from its initial value, 0.

At the other boundaries the offset terms are evaluated according to the formulas:

$$\hat{p}^{n+1}_{1-1,j} = \hat{p}^{n}_{2j} - 2\Delta x\left(\frac{\partial \hat{p}}{\partial x}\right)_{1j} \qquad \text{at } i = 1, \qquad (4.5.8)$$

$$\hat{p}^{n+1}_{i1-1} = \hat{p}^{n}_{i2} - 2\Delta y\left(\frac{\partial \hat{p}}{\partial y}\right)_{i1} \qquad \text{at } j = 1, \qquad (4.5.9)$$

and

$$\hat{p}^{n}_{ij+1} = \hat{p}^{n}_{i,N_{j-1}} + 2\Delta y\left(\frac{\partial \hat{p}}{\partial y}\right)_{iN_j} \qquad \text{at } j = N_j, \qquad (4.5.10)$$

where the partial derivatives are given by the boundary conditions, equations (4.5.4) through (4.5.6). This method of applying the derivative boundary conditions is second-order accurate in Δx and Δy as is the centered differencing used at interior points. A more popular derivative boundary technique which calculates the boundary values directly as, for example,

$$\hat{p}^{n+1}_{11} = \hat{p}^{n+1}_{12} - \Delta y\left(\frac{\partial p}{\partial y}\right)_{11},$$

cannot be applied to the present problem because it would introduce an inconsistency at the corners $(x_L, 0)$ and (x_L, L) where a normal derivative condition meets a pressure condition. Although the latter technique is easier to apply and has a heuristically pleasing form, its use would lead to significant numerical error in V_x near the corners.

The strategy developed by B. A. Carre' in reference 10 is used to estimate the optimum value of the relaxation parameter ω. Use of the optimum ω was observed to reduce the number of iterations in the SOR technique by a factor of ten to fifteen over use of $\omega=1$, the Gauss-Seidel scheme. The optimal ω is estimated dynamically during solution for $\hat{p}$ as follows:

1. Choose an initial ω in the range $1<\omega<\omega_o$ where ω_o is the (unknown) optimal value of ω.
2. Perform N iterations on equation (4.5.7).
   After the N^{th} iteration set

$$r^{(n)} = \sum_{j=1}^{N_j}\sum_{i=1}^{N_i}\left|\hat{p}^{(n)}_{ij} - \hat{p}^{(n-1)}_{ij}\right|$$

   for n = N-1 and n = N,

and $\lambda = r^{(N)} / r^{(N-1)}$.

3. The optimum ω is approximately

$$\omega_o \cong 2\left\{1 + \left[1 - \frac{\lambda+\omega-1}{\lambda\omega^2}\right]^{\frac{1}{2}}\right\} - 1.$$

4. Set $\omega = \omega_o - \frac{1}{4}(2-\omega_o)$

5. Repeat steps 2 through 4 until ω_o stops changing: $\frac{\Delta\omega_o}{2-\omega_o} < .05$.

6. Continue iterating on equation (4.5.7) with $\omega=\omega_o$ until $\hat{p}$ converges.

The values of ω and N in steps 1 and 2 are taken as $\omega=1.375$ and N=12.

The convergence test on $\hat{p}$ checks the largest relative change in $\hat{p}$ over each iteration until

$$\max_{i,j}\left[\left|\hat{p}_{ij}^{(n)} - \hat{p}_{ij}^{(n-1)}\right| / \tfrac{1}{2}\left(\left|\hat{p}_{ij}^{(n)}\right| + \left|\hat{p}_{ij}^{(n-1)}\right|\right)\right] < e_{SOR} \qquad (4.5.11)$$

where e_{SOR} is controlled by the progress of the steady-state solution as described in section 4.8. If condition (4.5.11) is not obtained within M_{SOR} iterations, an error message is displayed and the calculation proceeds to step 7.

An initial $\hat{p}$ distribution is needed to start the SOR iterations. Although the initial $\hat{p}$ does not affect the final pressure solution, a substantial savings in computing time can be achieved by starting with a good initial estimate. During the first iteration on the steady-state solution the analytic zero-gravity solution is used to start the pressure iterations; for subsequent steady-state iterations the final $\hat{p}$ distribution from the previous steady-state iteration is used. In the zero-gravity case $V_y=0$, so $\hat{p}$ can be calculated by solving Darcy's Law, equation (4.6.1), for $\frac{\partial\hat{p}}{\partial x}$ and integrating it across the S/L zone:

$$\hat{p}\ (x,y) = 0 + \int_{x_L}^{x} \left(-\frac{\mu g_L}{K} V_x\right) dx \qquad (4.5.12)$$

V_x for the zero gravity case is given by equation (4.3.2).

All procedures described in this subsection are coded in subroutine PSOLVE except the initial estimated $\hat{p}$ which is calculated in subroutine EST.

4.6 VELOCITY CALCULATION

After the pressure distribution is known, the velocity can be evaluated directly from Darcy's Law, equation (3.6.9), written in terms of $\hat{p}$:

$$\vec{V} = -\frac{K}{\mu g_L}(\nabla\hat{p} + (\rho_L - \rho_{Lo})\vec{g}). \qquad (4.6.1)$$

At interior points the gradient term is replaced by centered finite differences:

$$\left(\frac{\partial\hat{p}}{\partial x}\right)_{ij} \cong \frac{\hat{p}_{i+1,j} - \hat{p}_{i-1,j}}{2\Delta x} \text{ for } 1<i<N_i \text{ and } 1\leq j\leq N_j,$$

and $\left(\frac{\partial\hat{p}}{\partial y}\right)_{ij} \cong \frac{\hat{p}_{i,j+1} - \hat{p}_{i,j-1}}{2\Delta y}$ for $1\leq i\leq N_i$ and $1<j<N_j$.

First order one-sided differences of the form (4.4.6) are used at x_L while the boundary conditions provide values for the remaining pressure gradient terms.

Velocity is calculated in subroutine VLCTY: K is evaluated in subroutine PERM.

4.7 SOLUTION OF THE LOCAL SOLUTE REDISTRIBUTION EQUATION

After the velocity field is known g_L can be calculated by solving the local solute redistribution equation. In the steady-state case this can be simplified to an integration along lines of constant y. The steady-state hypothesis, equation (3.5.2), applied to equation (3.6.1) gives

$$\frac{1}{g_L}\frac{\partial g_L}{\partial X} = -\left[\frac{1}{1-k}\frac{\rho_L}{\rho_S}\left(1 + \frac{\vec{V}\cdot\nabla T}{\frac{\partial T}{\partial t}}\right)\right]\frac{1}{C_L}\frac{\partial C_L}{\partial} . \qquad (4.7.1)$$

Then g_L is approximated by

$$(g_L)_{ij} = (g_L)_{i+1,j}\left[\frac{(C_L)_{ij}}{(C_L)_{i+1,j}}\right]^{-\bar{q}} \qquad (4.7.2)$$

with $(g_L)_{N_i,j} = 1$, $\bar{q} = \frac{1}{2}(q_{ij} + q_{i+1,j})$,

and q_{ij} defined as the quantity in brackets in equation (4.7.1). After g_L is known, $\partial g_L/\partial t$ is calculated by a direct evaluation of equation (3.6.1).

g_L and $\partial g_L/\partial t$ are calculated in subroutine LFRAC.

4.8 ITERATION TO THE STEADY-STATE SOLUTION

At the end of each iteration on the steady-state solution, steps 5 through 9 in Section 4.2, g_L is tested for convergence. The convergence criterion is a comparison of the maximum relative change with an input threshold:

$$\max_{i,j}\left[\left|g_L^{(m)} - g_L^{(m-1)}\right| / \tfrac{1}{2}\left(g_L^{(m)} + g_L^{(m-1)}\right)\right] < E_{SSI} \qquad (4.8.1)$$

where $g_L^{(m)}$ is g_L at the end of the m^{th} iteration. If condition (4.8.1) is not obtained by the end of M_{SSI} iterations an error message, "steady-state solution did not converge" is put on the screen and the iteration process is terminated. E_{SSI} and M_{SSI} are user-specified inputs as described in Volume III.

The convergence threshold for the pressure iteration, e_{SOR}, is controlled by the progress of the steady-state iteration. Initially the pressure convergence threshold is 10 E_{SOR}, when the left side of inequality (4.8.1) drops below 100 E_{SSI}, e_{SOR} is reduced to 5 E_{SOR}, and when the left side of (4.8.1) is below 10 E_{SSI}, e_{SOR} is equal to E_{SOR}. This strategy speeds up the calculation by avoiding unnecessarily tight convergence of the pressure equation while g_L is relatively far from its steady-state value.

Iteration to the steady-state solution is controlled by subroutine SSICON.

4.9 CALCULATION OF MACROSEGREGATION

The integral in equation (3.6.15) can be transformed to an integral with respect to the logarithm of g_L:

$$\int_{x_L}^{x_E} kC_L\,dg_s = \int_{x_E}^{x_L} kC_L\,dg_L = \int_{x_E}^{x_L} kC_L g_L\,d(\ln g_L). \qquad (4.9.1)$$

Accurate numerical evaluation of the second integral in (4.9.1) would require an extremely fine mesh for alloy systems such as Sn-Bi whose large k causes g_L to be steep near the liquidus isotherm. The last integral in (4.9.1) is amendable to accurate approximation on a relatively small mesh. It is approximated as

$$\int_{x_E}^{x_L} kC_L g_L d(\ln g_L) \simeq \sum_{i=2}^{N_I} k\frac{1}{2}\left[(C_L g_L)_i + (C_L g_L)_{i-1}\right]\left[\ln g_{L_i} - \ln g_{L_{i-1}}\right]; \quad (4.9.2)$$

the remaining terms in (3.6.15) are evaluated directly, with g_E equal to g_L at i=1.

$\overline{C}_s$ is evaluated in subroutine MACSEG.

4.10 FRECKLE CONDITION

The existence of freckling in a given case can be detected by the program. The freckling condition is local remelting:

$$\frac{\partial T}{\partial t} = \frac{\partial T}{\partial t} + \vec{V}\cdot\nabla T > 0 \quad (4.10.1)$$

When condition (4.10.1) is detected at any point in the mesh, the calculation is stopped.

The freckle condition is tested in subroutine FRECKL.

SECTION 5 - EVALUATION

This section presents and describes the results of calculations using the model for flow of interdendritic liquid and macrosegregation described in Sections 3 and 4. Calculations are for three alloys (Al-4.5% Cu, Sn-15% Pb, and Sn-3% Bi) which show the effects of varying (1) the height of the solid-liquid zone, (2) the gravity force, and (3) the cooling rate during solidification. Added discussion is given to the formation of "freckles" and to the differences in macrosegregation behavior among the three alloys.

Ingot Height

Figure 3.2 illustrates the solid-liquid (S/L) zone in a unidirectionally solidified horizontal ingot. The width of the S/L zone is $X_L - X_E$, and the height is L. Figure 5.1 shows the effect of ingot height on macrosegregation. As ingot height increases, the major effect is that segregation is reduced, particularly in the central portion of the ingot. Thus the taller the ingot, the greater is the portion of the ingot near C_o (the average composition of the alloy). In this regard, Figure 5.1 compares well with Figure 10 in reference 1. However, there are differences at the top and bottom of the ingot which are attributed to differences in the choice of finite difference equations used to formulate the boundary conditions at the top and bottom of the ingot and in the method of solving for the velocity of the interdendritic liquid. In this work, since velocity is sensitive to the volume fraction of liquid, then a scheme is used whereby an iteration calculation is done to solve for velocity. Algorithms used herein give results with improved accuracy of those given in Reference 1; details are given in Section 4 of this report.

Gravity Force

Figure 5.2 shows the effect of the gravity force on macrosegregation in Al-4.5% CU alloy. With zero gravity, there is no macrosegregation because flow of interdendritic liquid is solely due to solidification shrinkage. As such, all flow is normal to isotherms as shown in Figure 5.3a. The effect of gravity is to cause the flow to be downward within much of the S/L zone, and there is some reversal of flow in the lower right areas of Figures 5.3b and c. Notice, also, that the magnitude of the vectors increases with increasing gravity force. Figure 5.4 gives the solute flux corresponding to Figure 5.3 in terms of g of

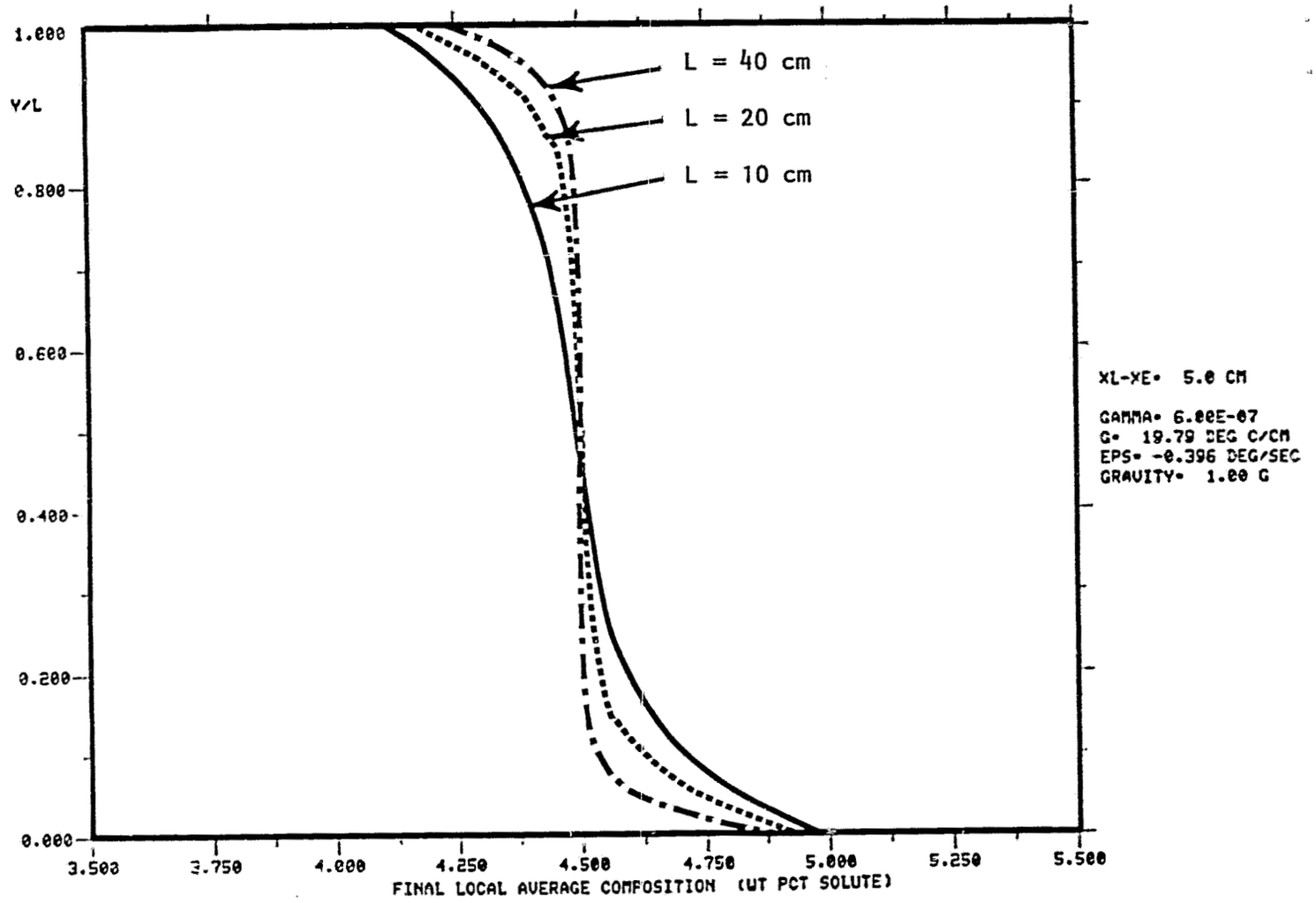

Figure 5.1. Effect of ingot height on macrosegregation.

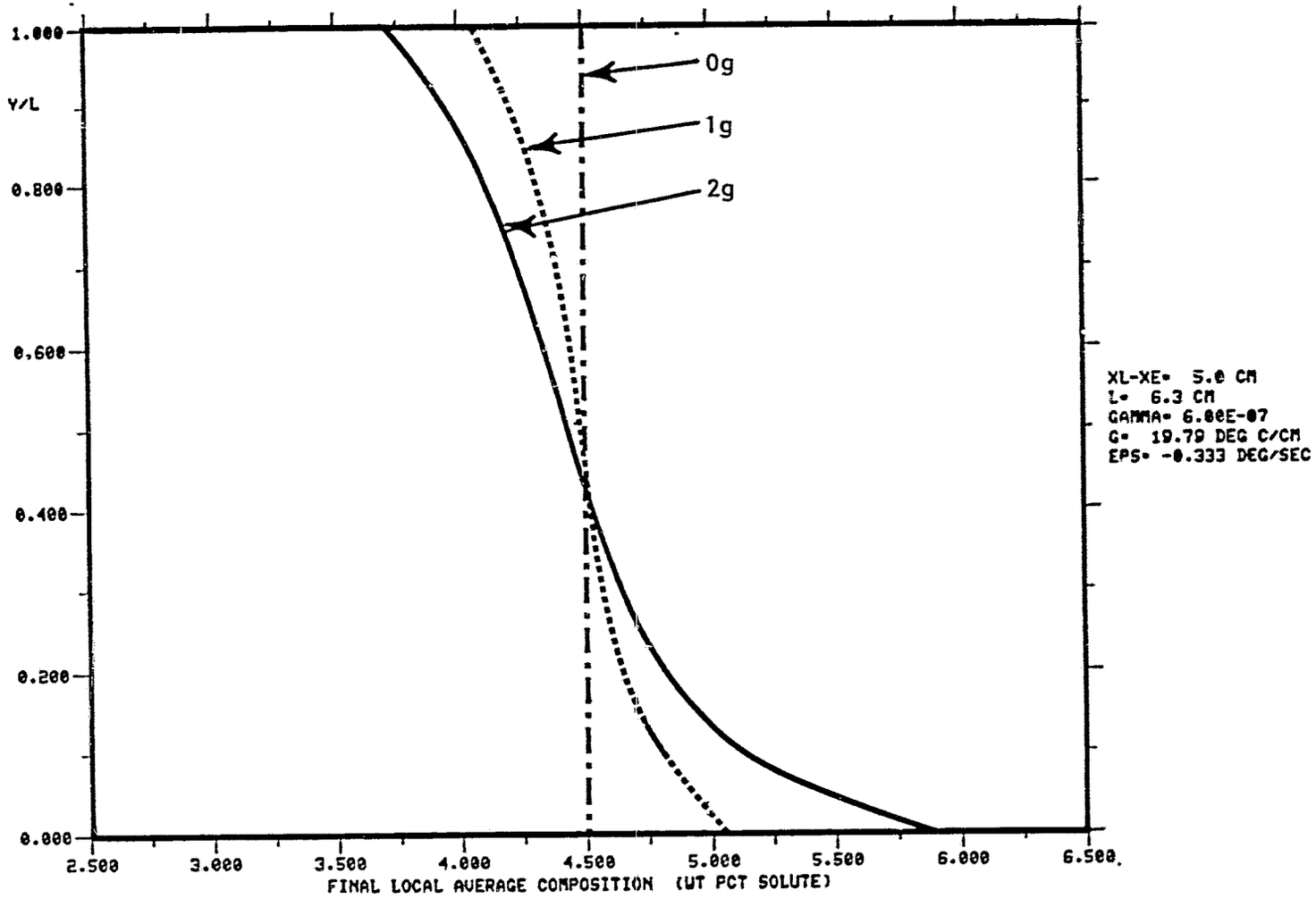

Figure 5.2. The effect of gravity force on Macrosegregation in Al - 4.5% Cu alloy.

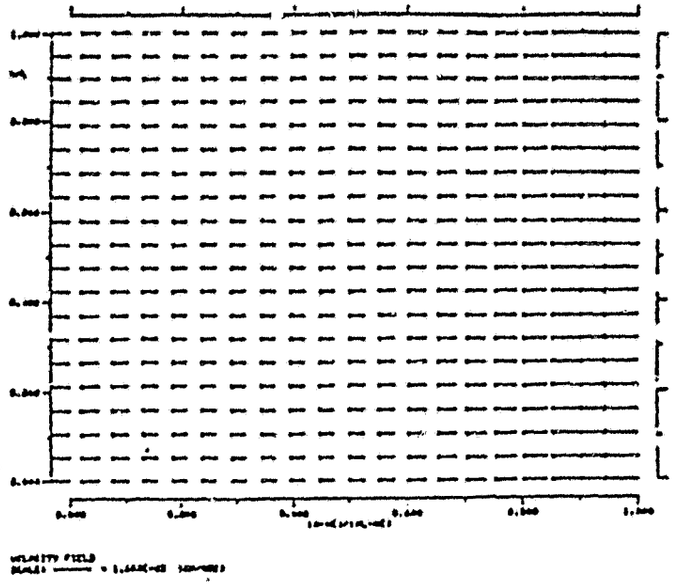

(a)

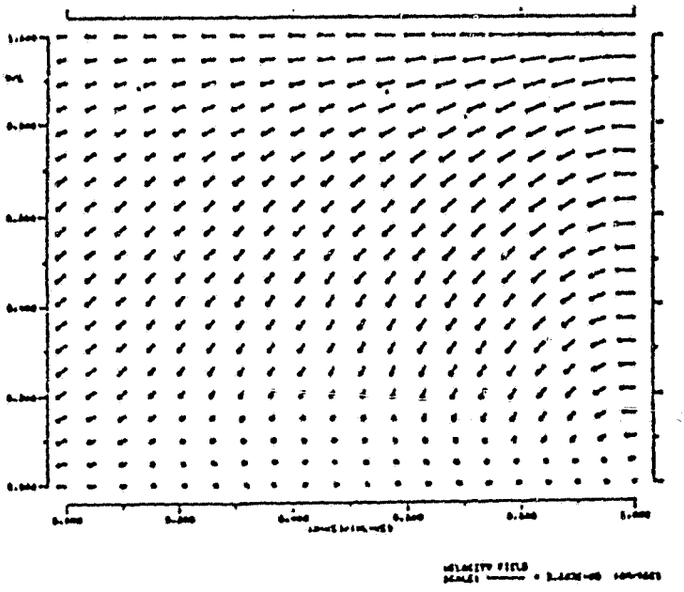

(b)

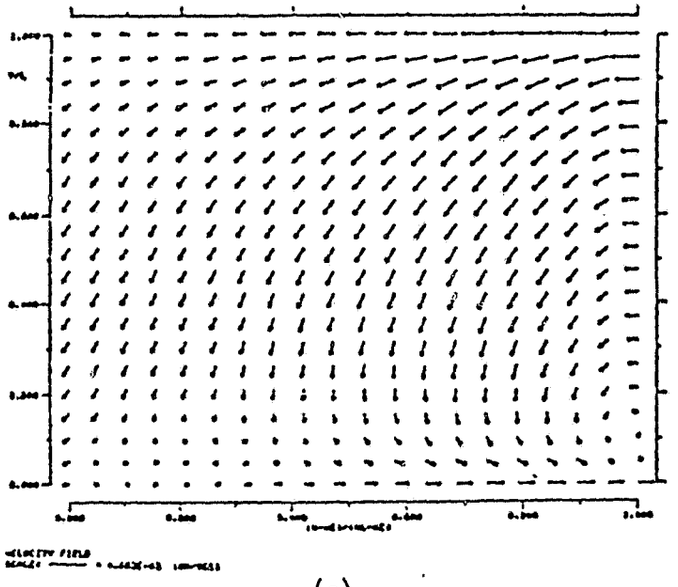

(c)

Figure 5.3. Effect of gravity on the velocity of interdendritic liquid in Al - 4.5% Cu: (a) 0 g; (b) i g; (c) 2 g. Conditions are the same as in Figure 5.2.

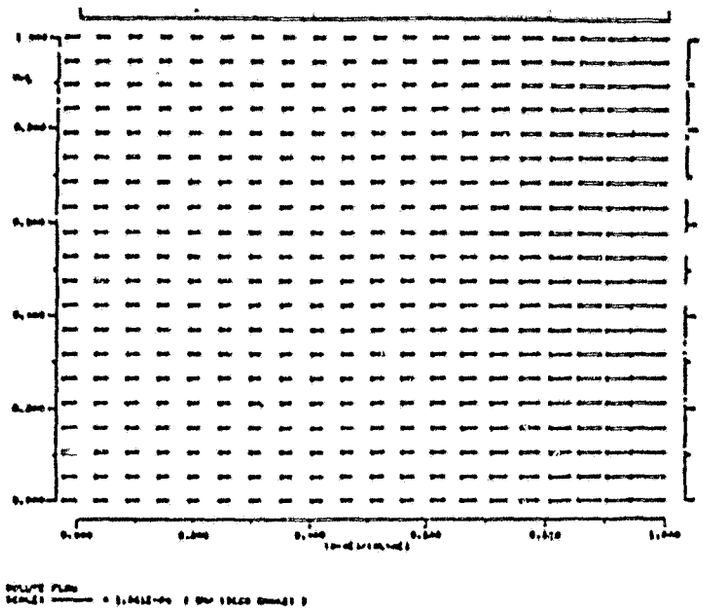

(a)

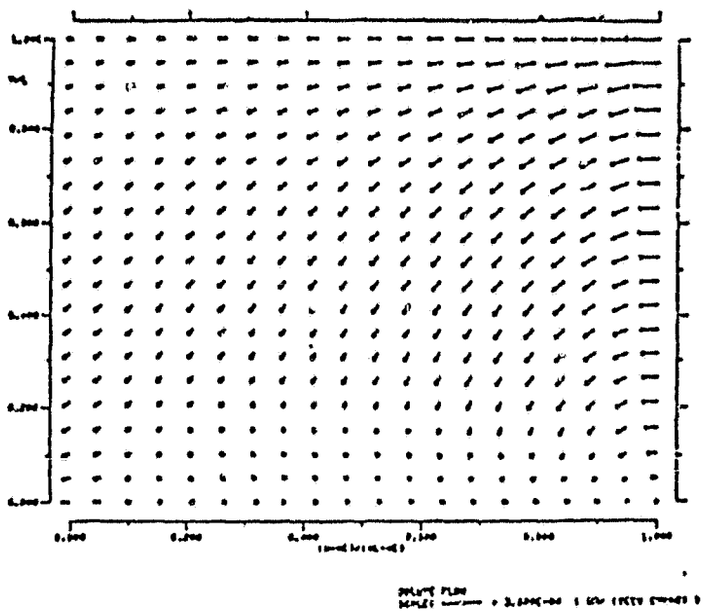

(b)

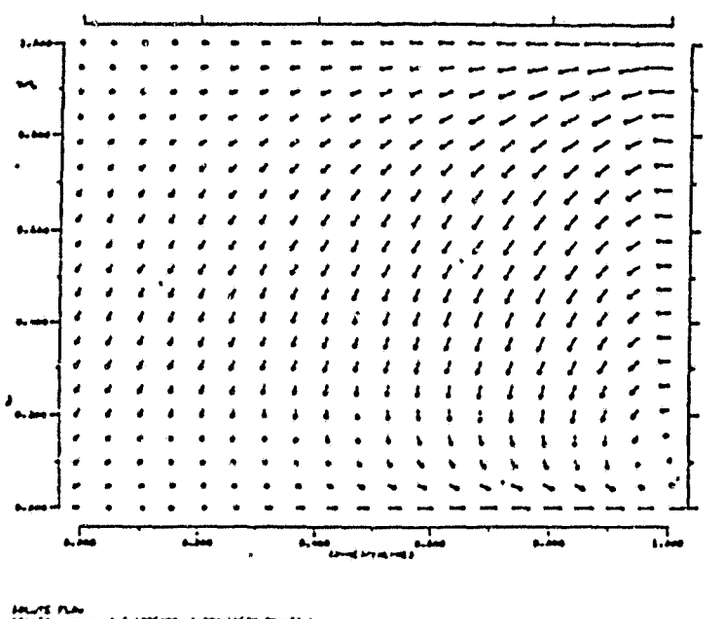

(c)

Figure 5.4. Effect of gravity on the solute flux in the interdendritic liquid in Al - 4.5% Cu Alloy: (a) 0g; (b) 1g; (c) 2g. Conditions are the same as in Figure 5.2.

Cu/s-cm^2. These fields are similar to those of Figure 5.2 and are given here to point out that this option for output is available. Figures 5.3 and 5.4 also show why segregation is negative at the top and positive at the bottom in Figures 5.1 and 5.2 when a gravity force acts on the liquid. Since the density of the liquid increases during solidification, the solute-rich liquid flows away from the upper portion towards the lower portion of the ingot (Figures 5.3 and 5.4) resulting in negative segregation at the top and positive segregation at the bottom. For alloys in which liquid density decreases during solidification, flow would be from bottom to top (opposite to Figures 5.3 and 5.4), and segregation profiles would be reversed from those shown in Figure 5.2.

Cooling Rate

For a given gravity force, the most important process variable, which influences macrosegregation, is cooling rate. This is shown in Figure 5.5 in which macrosegregation curves for lg at three different cooling rates have been drawn. One of the curves is that given in Figure 5.2 with a cooling rate of -0.333°C/S. When the cooling rate is doubled (-0.667°C/S), the segregation is substantially reduced. However, when the cooling rate is reduced to -0.100°C/S, segregation is increased significantly.

The effect of cooling rate on segregation can be explained by comparing the magnitudes of the velocity of interdendritic liquid and the isotherm velocities. With slow solidification, isotherms move slowly and there is more flow through a unit volume, within the mushy zone, during the time for complete solidification; thus macrosegregation is increased. Figure 5.6 shows this effect for the two extreme cooling rates of Figure 5.5. With the slower cooling rate (Figure 5.6a), the magnitude of the velocity of the interdendritic liquid is less than that at the greater cooling rate (Figure 5.6b), but relative to the velocity of the isotherms, there is substantially more flow at the lesser cooling rate. Consequently, macrosegregation increases with decreasing cooling rate as shown in Figure 5.5.

Formation of Freckles

When flow of interdendritic liquid is extensive and macrosegregation is severe, there is a reversal of that flow. This can be seen in the lower right areas of

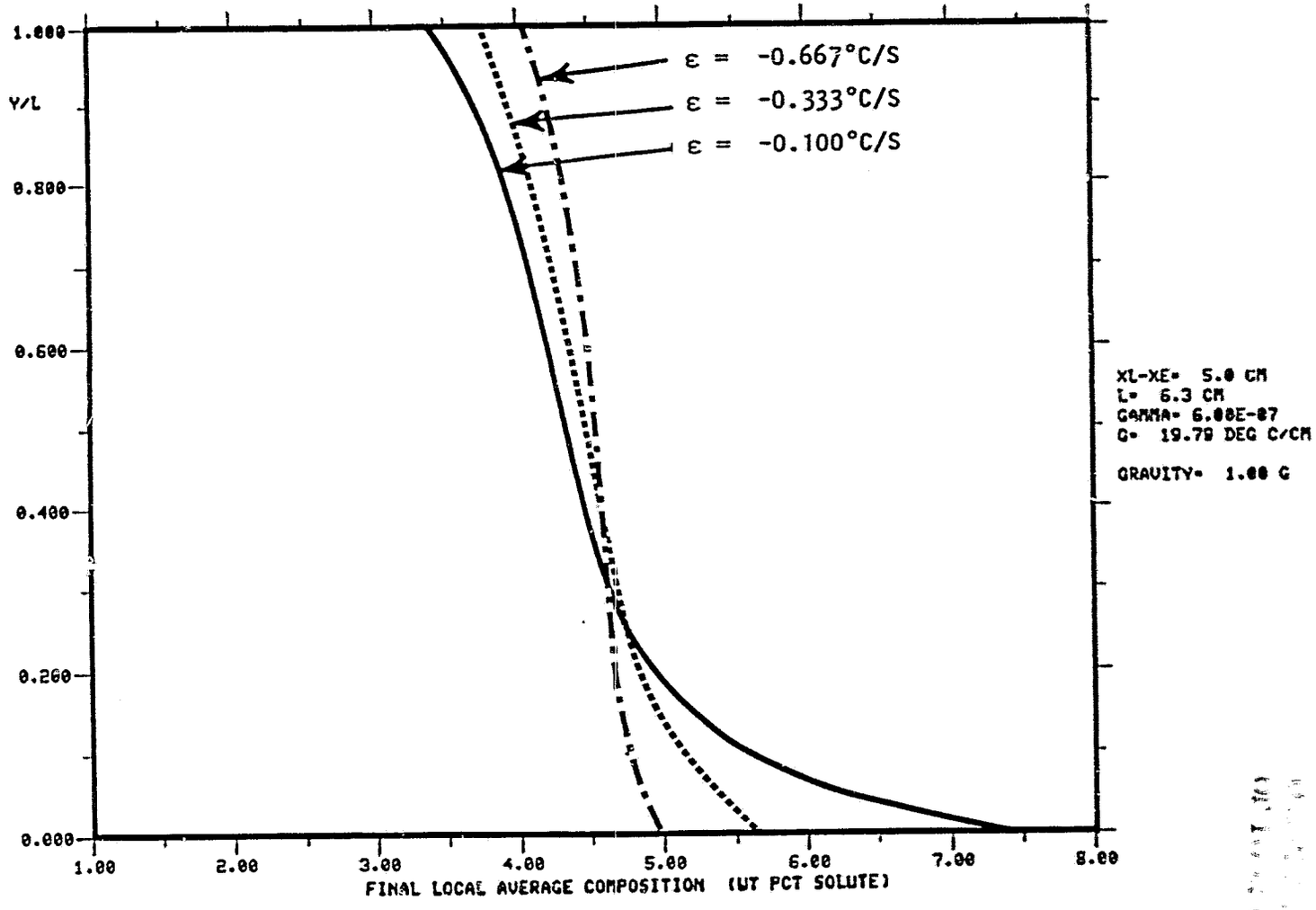

Figure 5.5. The effect of cooling rate, ε, on macrosegregation in Al - 4.5% Cu alloy.

(a)

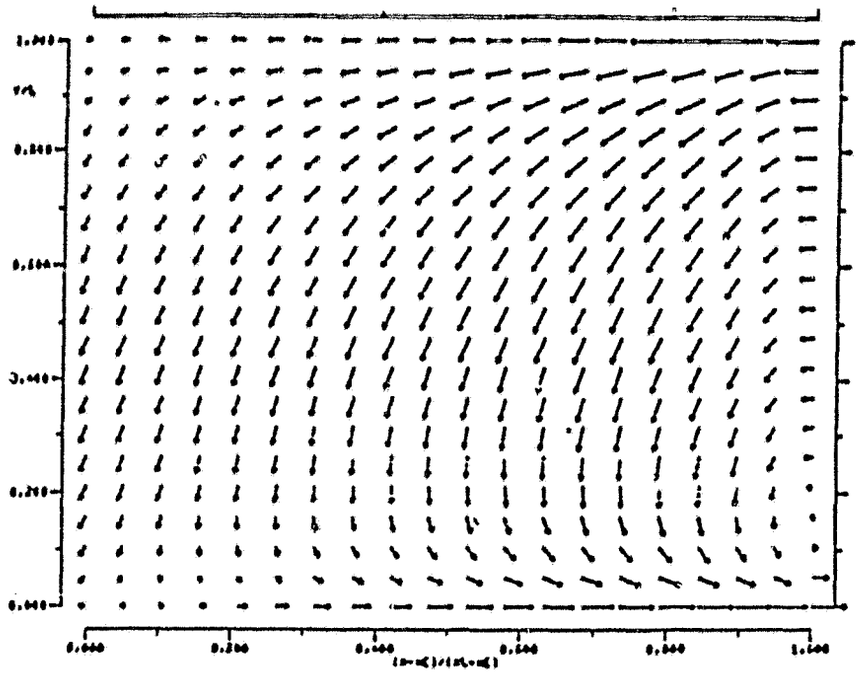

(b)

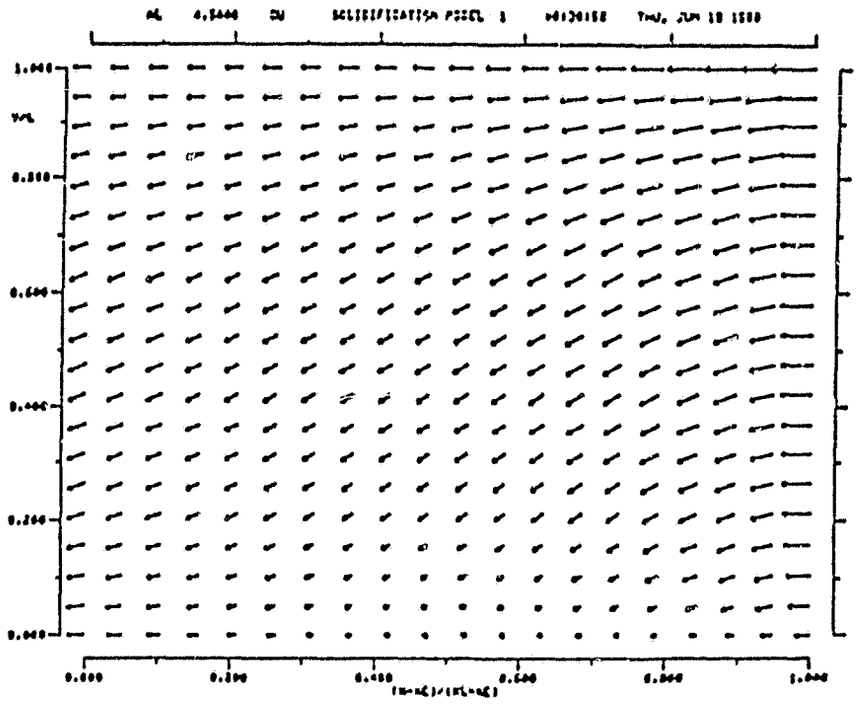

Figure 5.6. Effect of cooling rate on the velocity of interdendritic liquid in Al - 4.5% Cu: (a) -0.100°C/s, isotherm velocity is 5.05×10^{-3} cm/s; (b) -0.667°C/s, isotherm velocity is 3.37×10^{-2} cm/s. Conditions are the same as in Figure 5.5.

Figures 5.3c, 5.4c and 5.6a. There can be cases, which have been documented by experiment, in which the flow of the interdendritic liquid in the direction of the isotherms, exceeds the isotherm velocity. When this occurs, there is local remelting of the dendritic solid. The remelted region is the source of an unstable channel which persists within the solid-liquid zone and results in a severe localized segregate (i.e., "freckle") which is rich in eutectic constituent after solidification is complete. The criterion for this phenomenon is

$$(\vec{V}\cdot\nabla T/\varepsilon) \leq 1 \qquad (5.1)$$

where $\vec{V}$ is the velocity of the interdendritic liquid, ∇T is the temperature gradient and ε is the cooling rate. An alternative expression for equation (5.1) is

$$(\vec{n}\cdot\vec{V})/(\vec{n}\cdot\vec{U}) \geq 1 \qquad (5.2)$$

in which $\vec{n}$ is a unit vector normal to the isotherm and $\vec{U}$ is the velocity of the isotherm. Equation (5.2) essentially states that if the velocity of the liquid, in the direction of the moving isotherm, exceeds the velocity of the isotherm, then local remelting occurs. Equation (5.1) or equation (5.2) as an equality can be used to predict the onset of the formation of a freckle. However, if the inequality applies, then the model developed herein does not accurately predict macrosegregation.

In Figure 5.6a, the maximum value of the L.H.S of equation (5.2) is approximately 0.3; therefore, no freckles are predicted. For this particular ingot, the onset of freckling occurs at a cooling rate between $-0.033^{\circ}C/S$ and $-0.100^{\circ}C/S$.

Pressure Field

As discussed in Sections 3 and 4, calculation of the pressure in the solid-liquid zone is an intermediate step to compute the velocity of the interdendritic liquid. The major purpose of the analysis of macrosegregation is to calculate macrosegregation, as in Figures 5.1, 5.2 and 5.5; complementary information sought is often the velocity field of the interdendritic liquid as in Figures 5.3 and 5.6. There are circumstances, however, in which the pressure field would be of interest; one example would be to predict evolution of dissolved gas during solidification. Figures 5.7 (a) and (b) shows the pressure field corresponding to the velocity

(a)

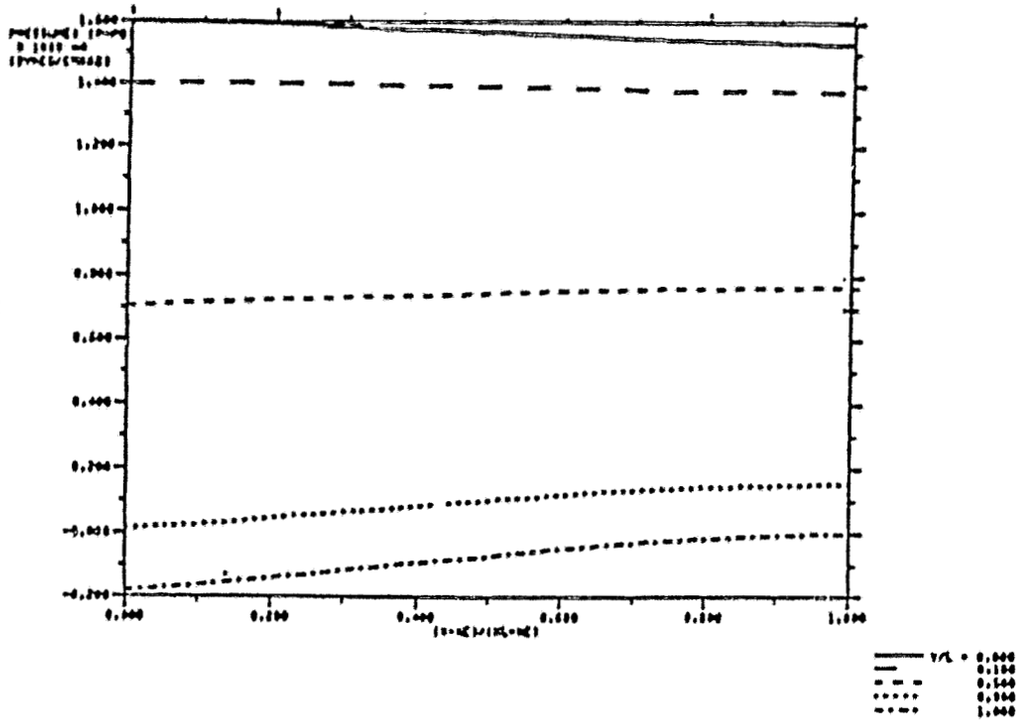

(b)

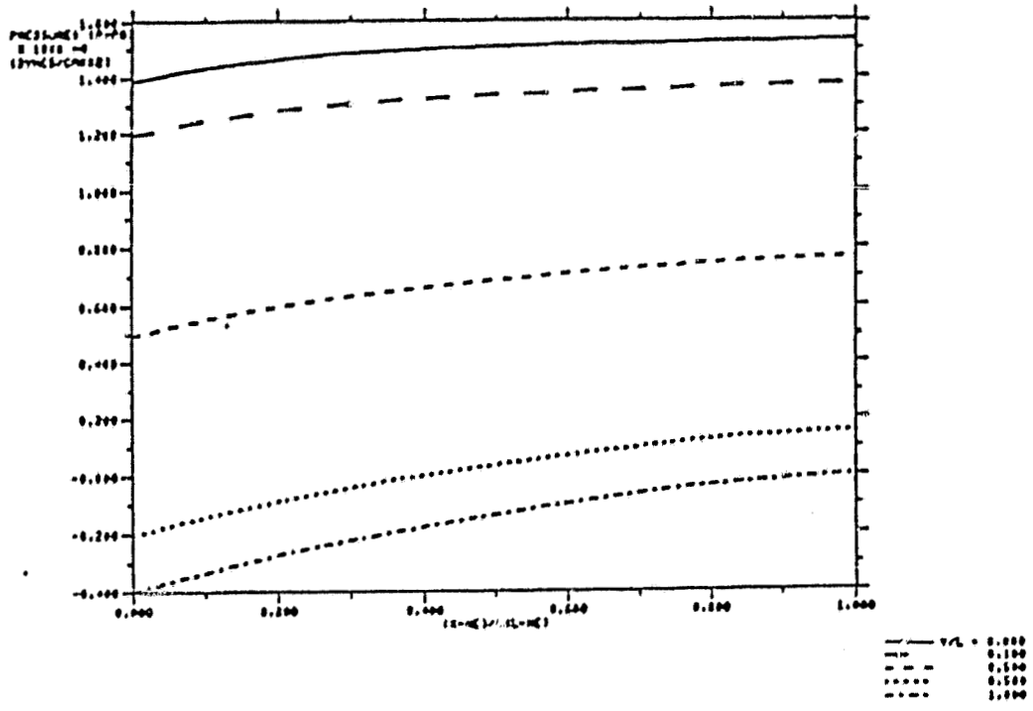

Figure 5.7. The pressure field in Al - 4.5% alloy for two cooling rates: (a) -0.100°C/s; (b) -0.667°C/s. Conditions are those described in Figure 5.5.

fields of Figures 5.6 (a) and (b), respectively. In Figures 5.7 (a) and (b), P_o is the ambient pressure at the top of the liquid pool (approximately 1 atm or 10^6 dynes/cm^2) and P is the pressure in the solid-liquid zone. Except at the bottom of the ingot solidified with a cooling rate of -0.100°C/s, there is a decrease of pressure through the solid-liquid zone. This pressure drop, of course, is attributed to the friction associated with flow of liquid through the dendritic network. As cooling rate increases, or permeability decreases, the pressure drop increases. For example, at $y/L = 0.5$, the pressure drop across the mushy zone for a cooling rate of -0.100°C/s is about 600 dynes/cm^2 (Figure 5.7a); at an increased cooling rate of -0.667°C/s, the pressure drop across the solid-liquid zone at $y/L = 0.5$ is about 2800 dynes/cm^2.

Other Alloys

Figures 5.8 and 5.9 show results for flow of interdendritic liquid and macrosegregation, respectively, in Sn-15% Pb alloy in an ingot of similar size as described above for Al-4.5% Cu alloy. In the Sn-Pb alloy, the volume fraction of liquid at the eutectic isotherm is approximately 3-4 times that in the Al-Cu alloy (0.35 vs. 0.09), so that the average volume fraction of liquid in the solid-liquid zone is also significantly greater in the Sn-Pb alloy than in the Al-Cu alloy. As a result, flow is very extensive in the Sn-Pb alloy (Figure 5.8) and much more so than shown in Figure 5.6. Hence, macrosegregation is also extensive as demonstrated by Figure 5.9 where there is a spread of 9% Pb from top to bottom of the ingot. Since the dendritic network of this ingot is so "open", then the pressure drop through the solid-liquid is almost non-existent; this is seen in Figure 5.10.

Finally, Sn-3% Bi alloy is an example of an alloy with a relatively minor amount of liquid (approximately 1-2%) at the eutectic isotherm. Also, it differs from Al-4.5% Cu alloy and Sn-15% Pb alloy in that there is an expansion on solidification near the end of freezing. Thus in Figure 5.11, the magnitude of the velocity vectors is about one order of magnitude less than in Figure 5.8, and the effect of expansion (rather than contraction) is apparent in the left side of the solid-liquid zone. Macrosegregation is only about 0.5% Bi from top to bottom in this ingot (Figure 5.12). The pressure field, Figure 5.13, is interesting in that the pressure "drop" is reversed corresponding to the direction of flow for much of the solid-liquid zone of Figure 5.11.

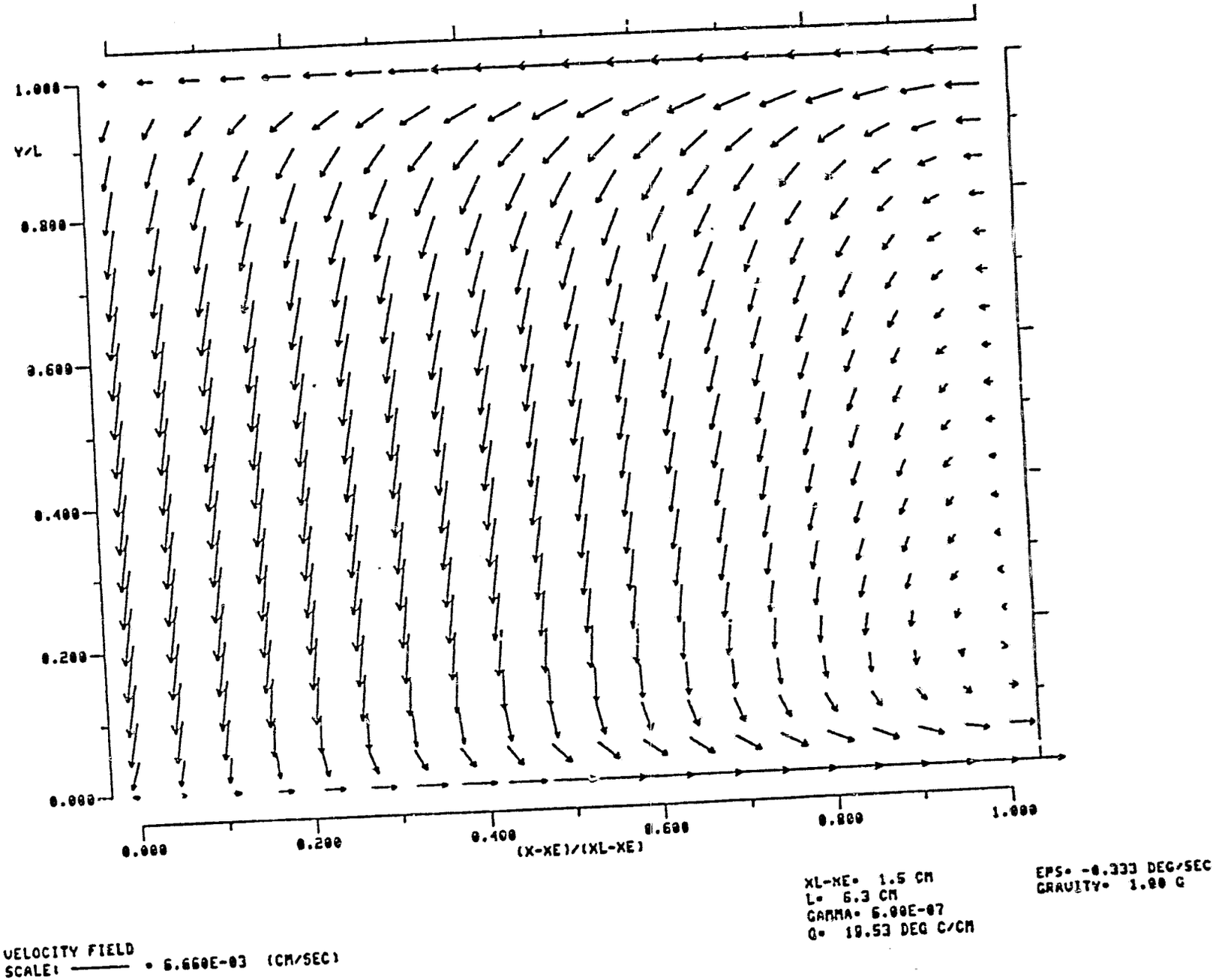

Figure 5.8. The velocity of interdendritic liquid in Sn-15% Pb alloy.

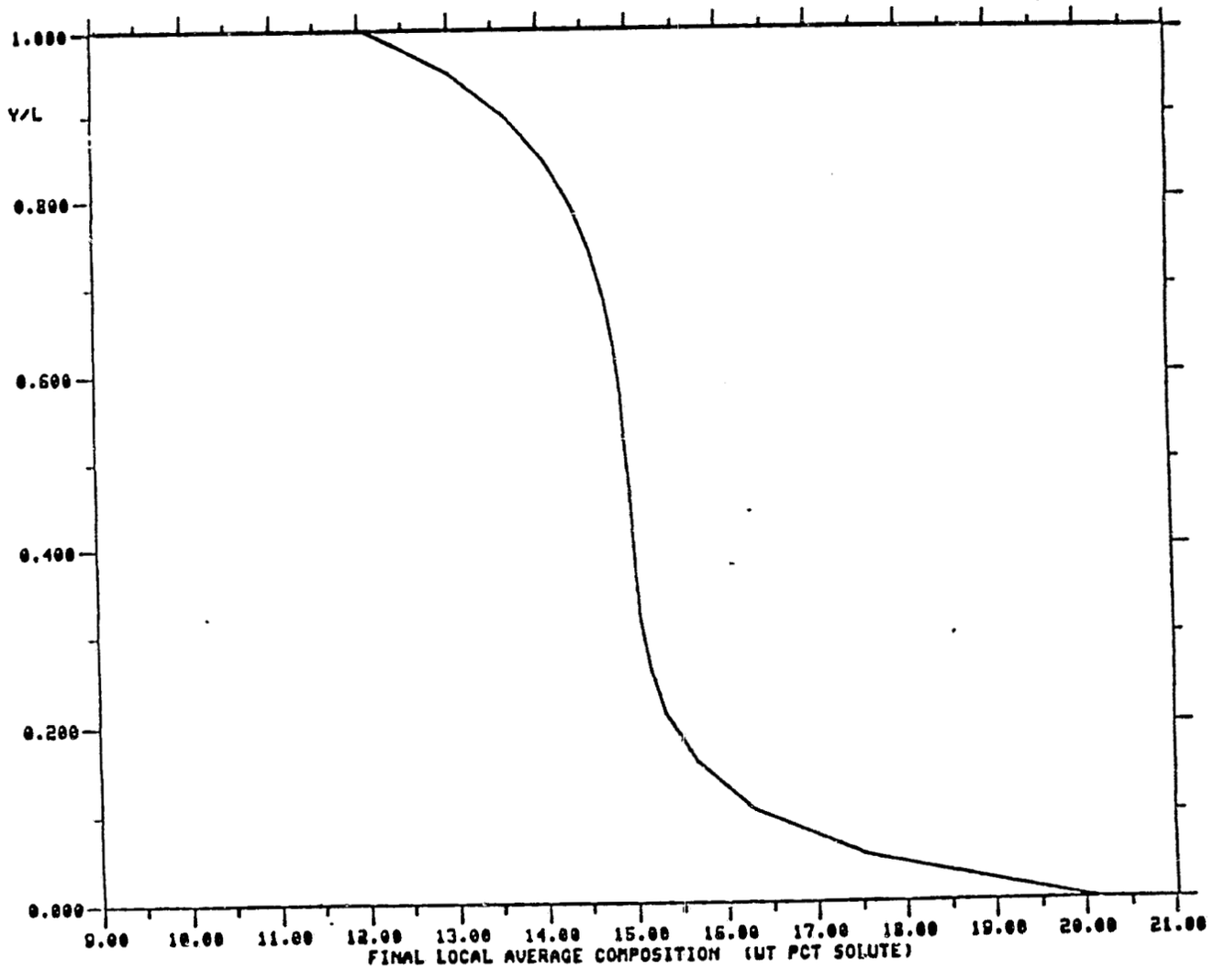

Figure 5.9. Macrosegregation in Sn - 15% Pb alloy. Conditions are the same as in Figure 5.8.

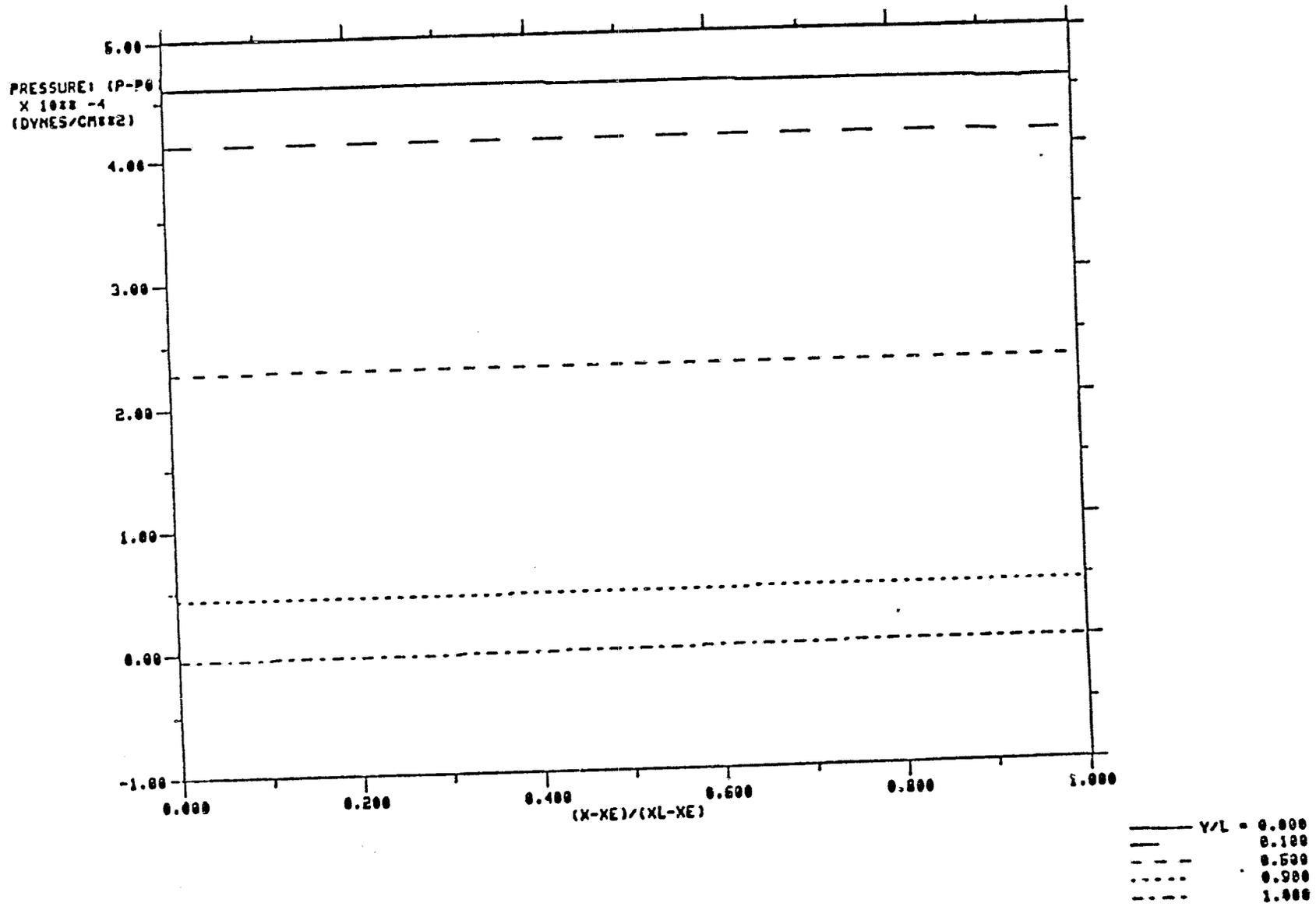

Figure 5.10. Pressure field in Sn - 15% Pb alloy. Conditions are the same as in Figure 5.8.

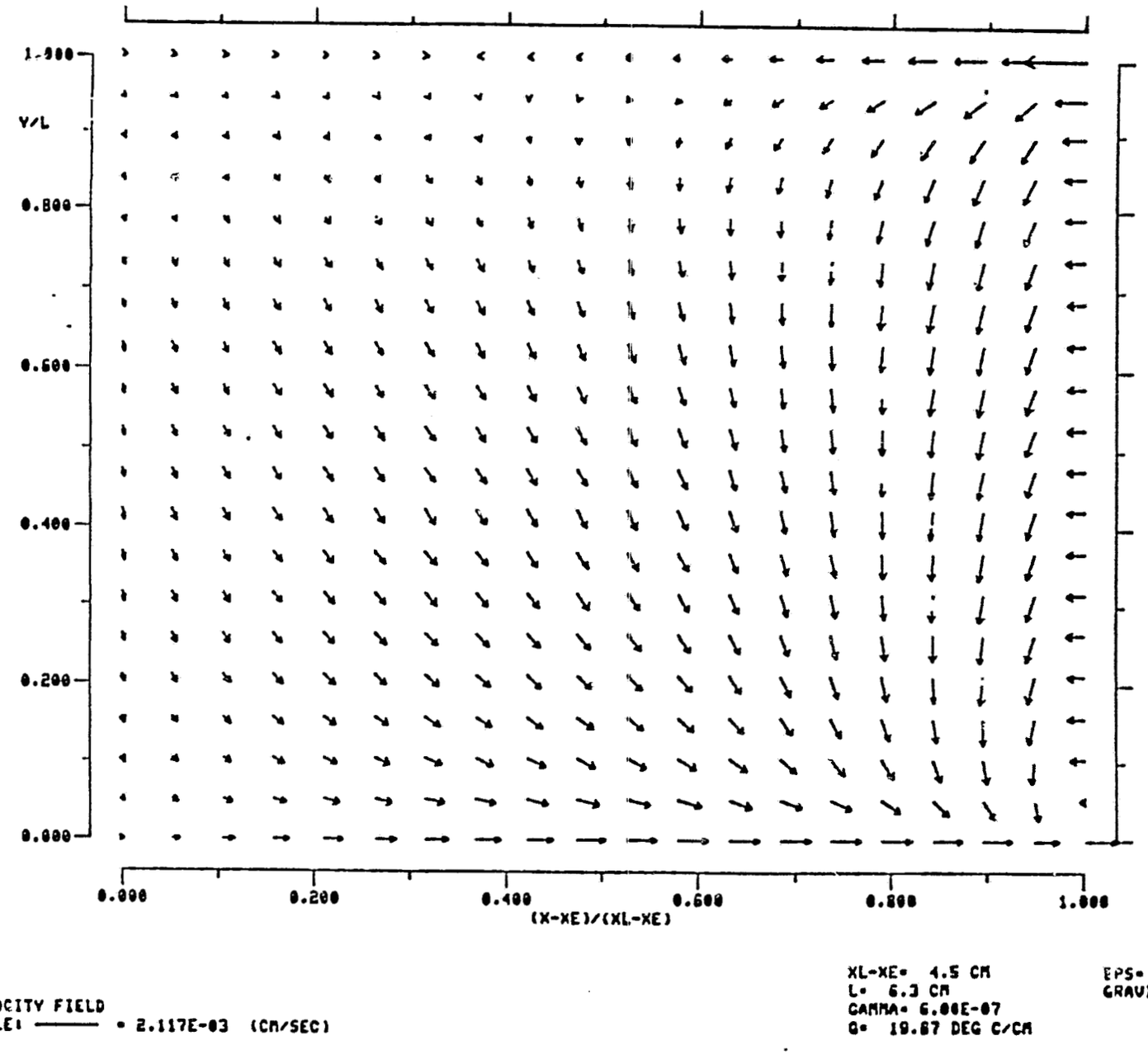

Figure 5.11. The velocity of interdendritic liquid in Sn - 3% Bi alloy.

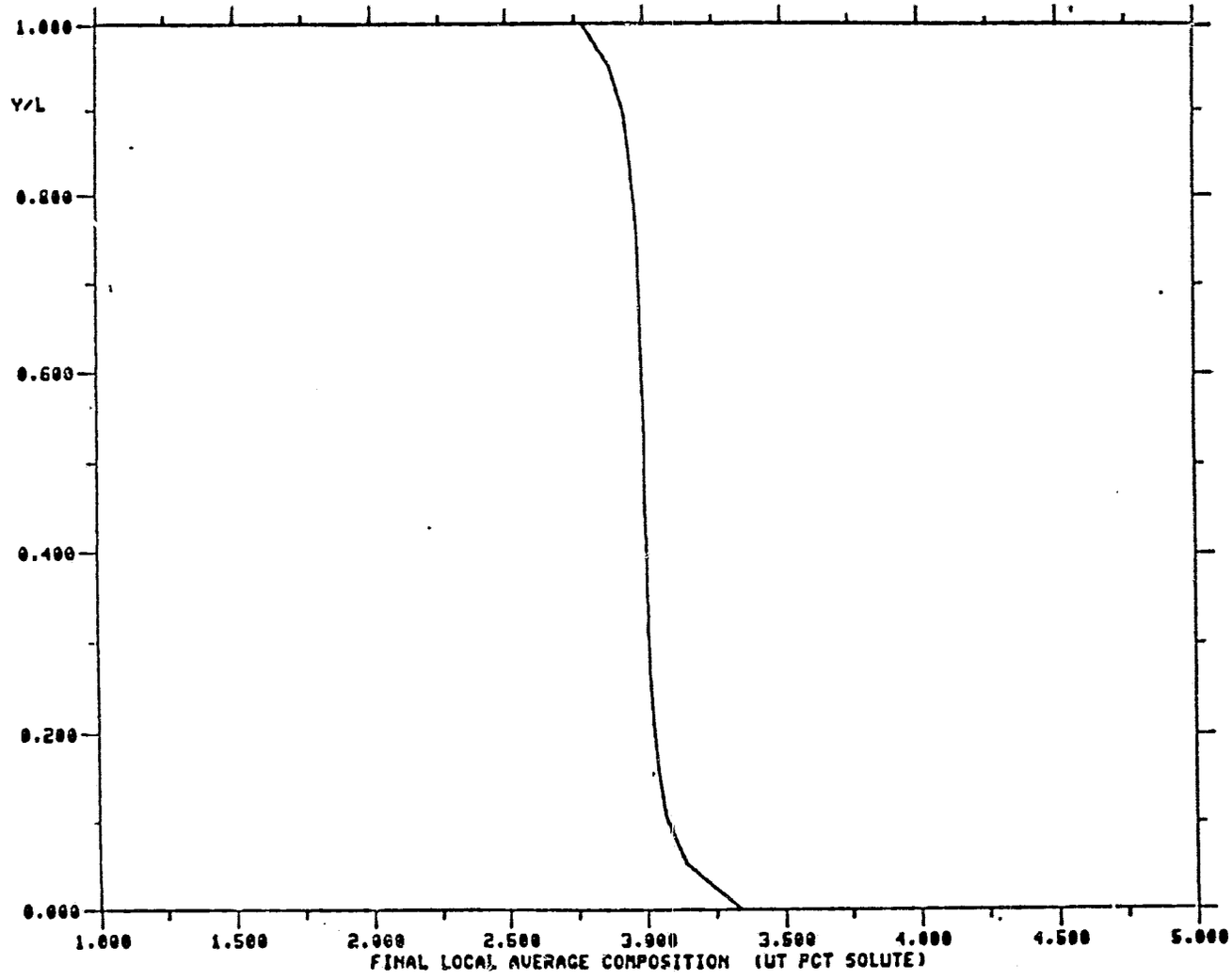

Figure 5.12. Macrosegregation in Sn - 3% Bi alloy. Conditions are the same as described in Figure 5.11.

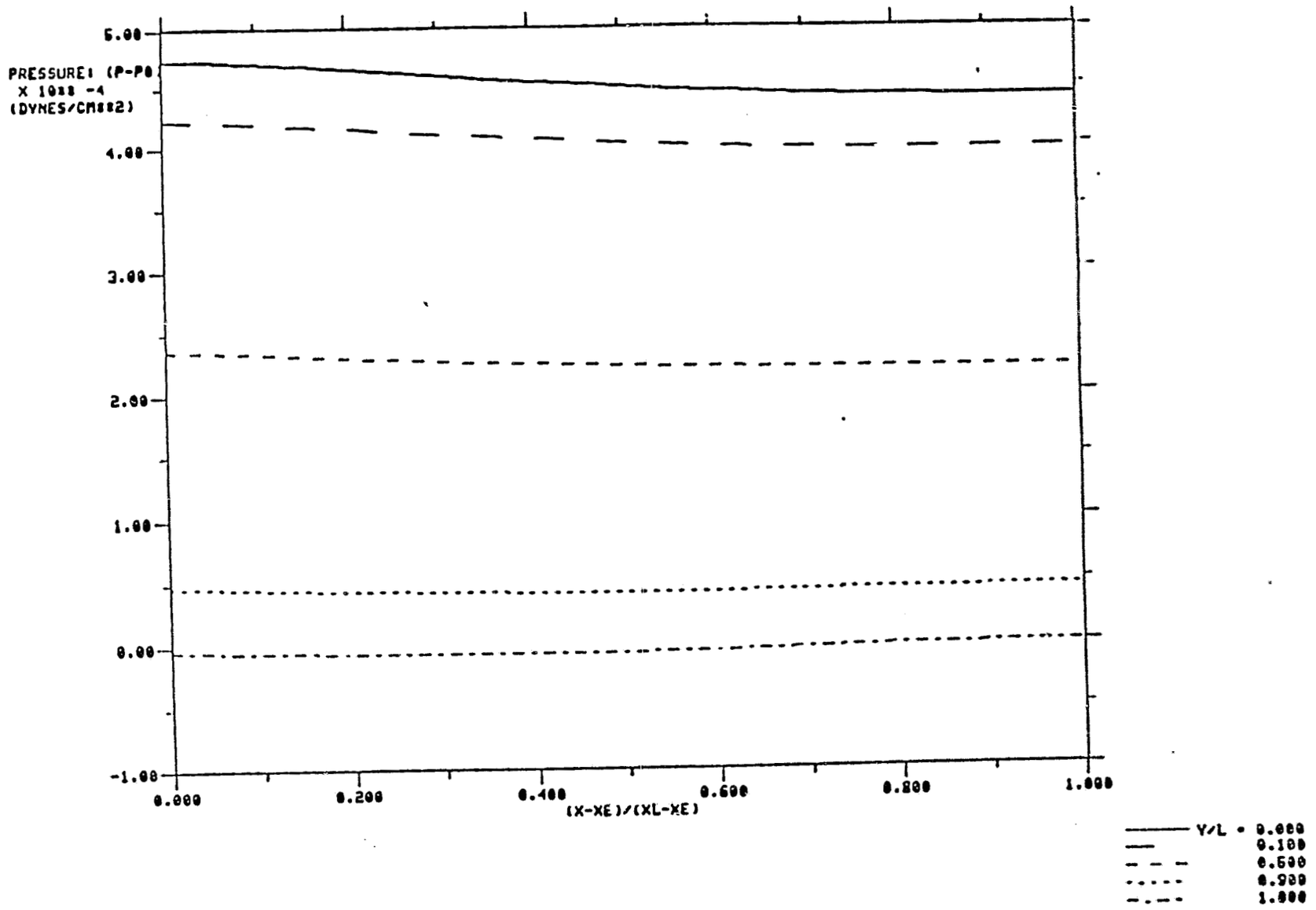

Figure 5.13. The pressure field in the solid-liquid zone of Sn - 3% Bi alloy. Conditions are the same as described in Figure 5.11.

SECTION 6 - REFERENCES

1. R. Mehrabian, M. Keane, and M. C. Flemings: Met. Trans., 1970, Vol 1, p. 1209.
2. S. Kou, D. R. Poirier, and M. C. Flemings: Proceedings of the Electric Furnace Conference, Iron and Steel Society of AIME, December, 1977.
3. M. C. Flemings and G. E. Nereo: Trans. TMS-AIME, 1967, Vol. 239, p. 1449.
4. M. C. Flemings, R. Mehrabian, and G. E. Nereo: Trans. TMS-AIME, 1968, Vol. 242, p. 41.
5. M. C. Flemings and G. E. Nereo: Trans. TMS-AIME, 1968, Vol. 242, p. 50.
6. R. Mehrabian, M. Keane, and M. C. Flemings: Met. Trans., 1970, Vol. 1, p. 3238.
7. S. M. Copley, A. F. Giamei, S. M. Johnson, and M. F. Hornbecker: Met. Trans., 1970, Vol. 1, p. 2193.
8. E. Isaacson and H. B. Keller: "Analysis of Numerical Methods", John Wiley & Sons, Inc., New York, 1966.
9. F. W. Dorr: SIAM Review, 1970, Vol. 12, p. 248.
10. B. A. Carré: Computer J., 1961, Vol. 4, p. 73.
11. Metals Handbook, Vol. 8, ASM, 1973.

APPENDIX A

ALLOY PROPERTIES AND SOLIDIFICATION PARAMETERS

Al-Cu System (References 1 and 3)

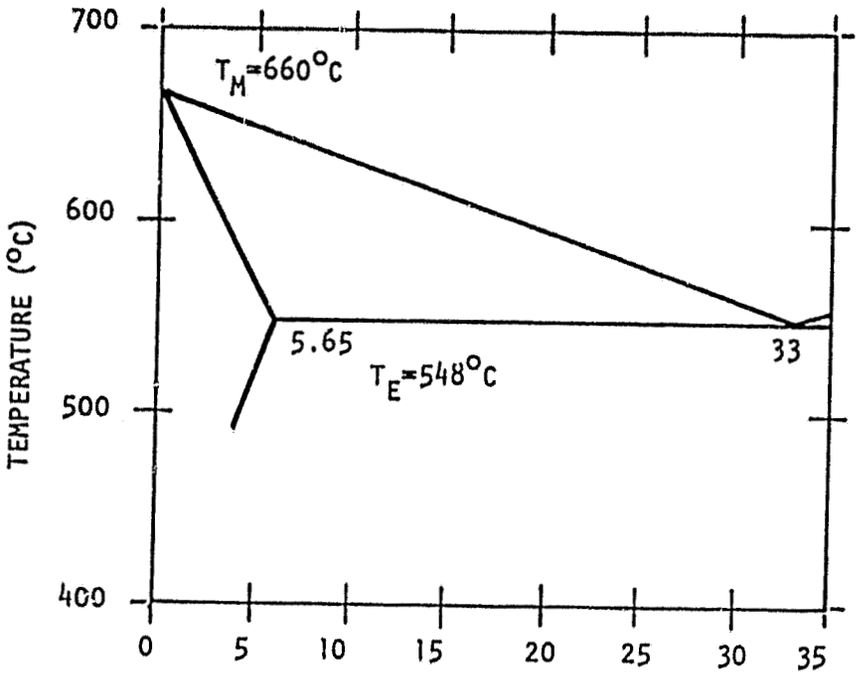

$$\frac{dC_L}{dT_L} = -.288 \frac{\%Cu}{^oC}$$

$$k = .172$$

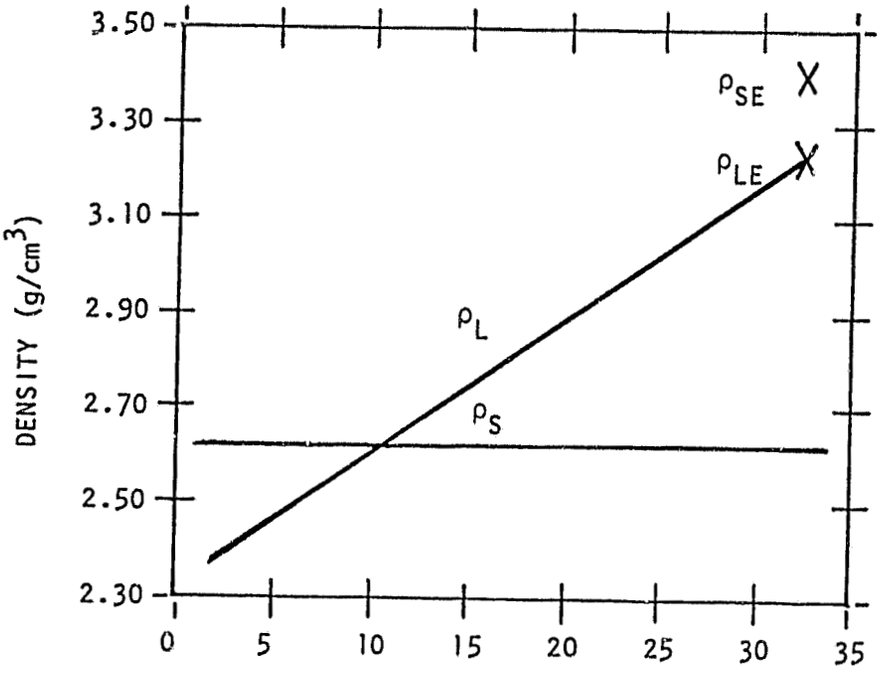

$\rho_{SE} = 3.40$ g/cm^3

$\rho_{LE} = 3.22$ g/cm^3

$$\frac{d\rho_L}{dC_L} = .0267 \frac{g/cm^3}{\%Cu}$$

$\rho_S = 2.62$ g/cm^3

$\mu = .03$ g/(cm·s)

Sn-Pb System (References 11 and 2)

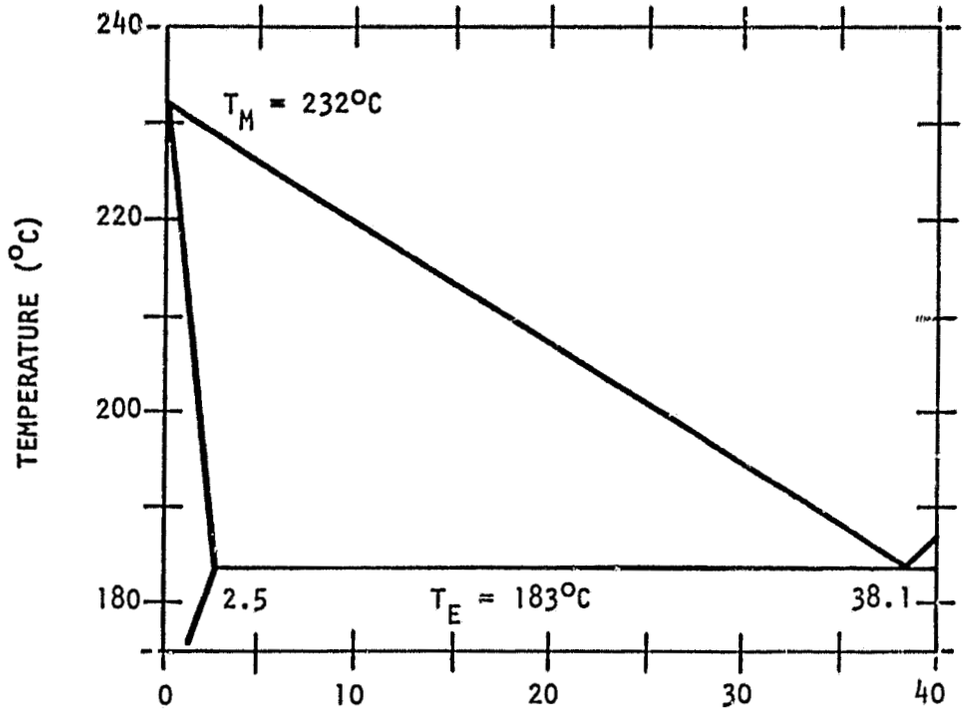

$$\frac{dC_L}{dT_L} = -.778 \frac{\%Pb}{°C}$$

$k = .0656$

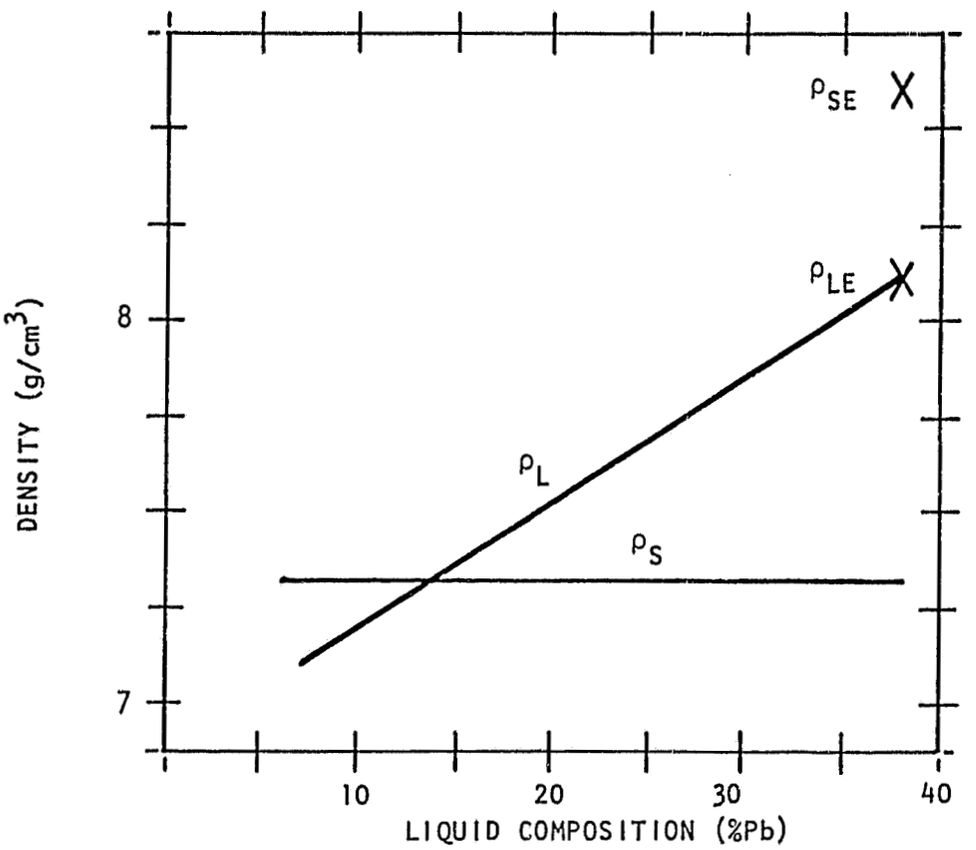

$\rho_{SE} = 8.59$ g/cm³

$\rho_{LE} = 8.10$ g/cm³

$$\frac{d\rho_L}{dC_L} = .0327 \frac{g/cm^3}{\%Pb}$$

$\rho_S = 7.30$ g/cm³

$\mu = .022$ g/(cm·s)
at C_o = 15% Pb

Sn-Bi System (See following discussion and Reference 11)

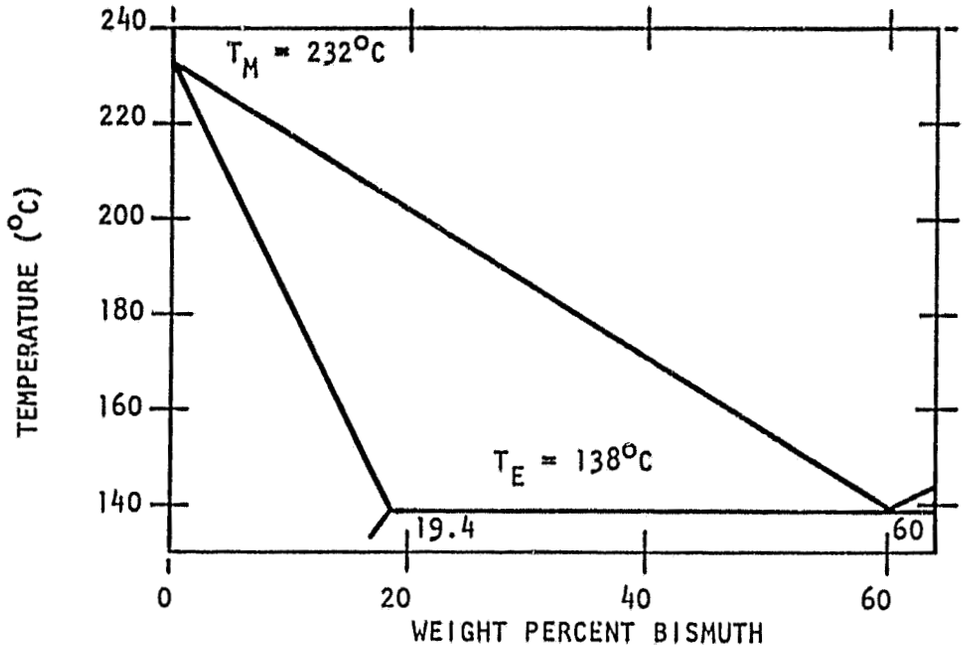

$$\frac{dC_L}{dT_L} = -.6382 \frac{\%Bi}{°C}$$

$$k = .3233$$

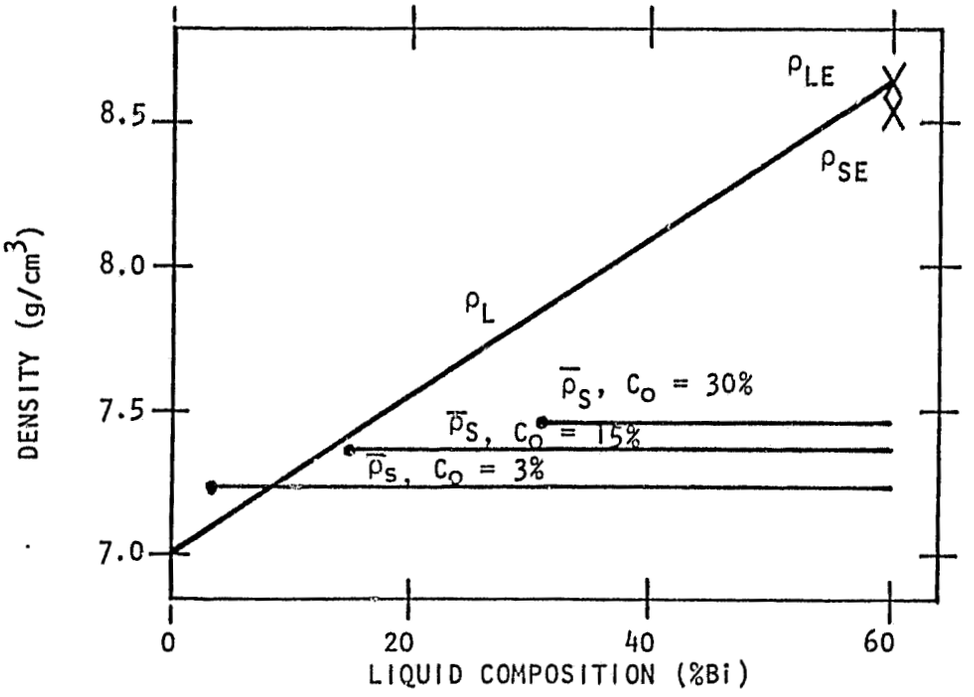

$\rho_{SE} = 8.60$ g/cm^3

$\rho_{LE} = 8.65$ g/cm^3

$$\frac{d\rho_L}{dC_L} = .0277 \frac{g/cm^3}{\%Bi}$$

$\rho_s = 7.24$ g/cm^3, C_o = 3% Bi
$= 7.36$ g/cm^3, C_o = 15% Bi
$= 7.46$ g/cm^3, C_o = 30% Bi

$\mu = .0215$ g/(cm-s), C_o = 3% Bi
$= .023$ g/(cm-s), C_o = 15% Bi
$= .024$ g/(cm-s), C_o = 30% Bi

Density of Solid

ρ_{SE} (density of eutectic solid) = 8.60 g/cm^3

ρ_S (Average density of solid) = 7.24 g/cm^3, C_o = 3% Bi
= 7.36 g/cm^3, C_o = 15% Bi
= 7.46 g/cm^3, C_o = 30% Bi

The density of the solid (tin rich - β phase) is determined using lattice spacing for pure Sn as a function of temperature, taken from Handbook of Lattice Spacings and Structure of Materials (HLSSM). The variation of density with temperature agrees exactly with that computed by using the thermal expansion coefficient given in Smithells, p. 941, and there is excellent agreement with the density (26°C) given in Handbook of Chemistry and Physics, 57th ed., CRC Press (HCP). The effect of Bi on the density of β - Sn is from HLSSM where the lattice spacings of β - Sn increase linearly with atom fraction Bi. At temperatures of the solidification range, the same variation is assumed.

For macrosegregation calculations, the average density of the "cored" solid phase is used; as such, the density of the solid depends upon the average composition of the solid. The average composition of the solid is estimated by the Scheil equation.

The density of eutectic solid is computed by using the density of Bi at 26°C and correcting for temperature with the thermal expansion coefficient (these data are in HCP). No data on the effect of Sn on density of Bi are available so the density of Bi - rich eutectic solid (98.4% Bi) is computed assuming ideal solution; i.e., the molar volume is given by the "law of mixtures".

Density of Liquid

$\rho_L = 0.0277\ C_L + 6.99$ g/cm^3

ρ_{LE} (density of eutectic liquid) = 8.65 g/cm^3

Density of liquid pure Sn is taken to be the average of data in Thresh and Crawley, Smithells and HCP all extrapolated to the solidification temperature range. In this range, the data from these sources agree well. For Bi four sets of data are in HCP and another in Smithells. Three sets of data which showed closer agreement were selected and averaged. However, whether 3 sets

or all 5 sets of data are considered makes little difference.

The density of liquid alloys was computed by assuming that the solutions are ideal; i.e., there are no volume changes due to solution and the "law of mixtures" applies. The procedure can be justified since the heat of mixing for these alloys is small indicating almost ideal behavior.

Viscosity

$$\mu = 1.583 \times 10^{-4} C_L + 0.0163$$

with μ in Poise (g/s-cm) and C_L is the composition along the liquidus (%Bi).

If constant values of μ are selected:

$\mu = .0215$ g/s-cm, $C_o = 3\%$ Bi

$= 0.023$ g/s-cm, $C_o = 15\%$ Bi

$= 0.024$ g/s-cm, $C_o = 30\%$ Bi

For pure Sn; Thresh and Crawley show that the viscosity obeys the Andrade equation; thus this is used as a basis to extrapolate the viscosity into the solidification temperature range. Viscosity data (from HCP) for pure Bi are reduced to the form of the Andrade equation and also extrapolated to the solidification temperature range. Viscosity of alloys is assumed to follow the "law of mixtures".